On Equivalent Circuit Modeling for Lithium-ion Batteries Operating over Broad Current Ranges

By

Nikhil Biju

B.S., University of Kansas, 2019

Submitted to the graduate degree program in Mechanical Engineering and the Graduate Faculty of the University of Kansas in partial fulfillment of the requirements for the degree of Master of Science.

Chair: Dr. Huazhen Fang

Dr. Gibum Kwon

Dr. Rajesh Rajamani

Date defended: April 28, 2023

The Thesis Committee for Nikhil Biju certifies
that this is the approved version of the following thesis :

On Equivalent Circuit Modeling for Lithium-ion Batteries Operating over Broad Current Ranges

Chair: Dr. Huazhen Fang

Date approved: May 08, 2023

Abstract

Advanced battery management is as important for lithium-ion battery systems as the brain is for the human body. Its performance rests on the use of fast and accurate battery models. However, the mainstream equivalent circuit models and electrochemical models have yet to meet this need well, due to their struggle with either predictive accuracy or computational complexity. This problem has acquired urgency as some emerging battery applications running across broad current ranges, e.g., electric vertical take-off and landing aircraft, can hardly find usable models from the literature. Motivated to address this problem, we develop an innovative model in this study. Called *BattX*, the model is an equivalent circuit model that draws comparisons to a single particle model with electrolyte and thermal dynamics, thus combining their respective merits to be computationally efficient, accurate, and physically interpretable. The model design pivots on leveraging multiple circuits to approximate major electrochemical and physical processes in charging/discharging. Given the model, we develop a multipronged approach to design experiments and identify its parameters in groups from experimental data. Simulation and experimental validation proves that the BattX model is capable of conducting accurate voltage prediction for charging/discharging across low to high C-rates.

Acknowledgements

My parents and I moved to Kansas from India when I was 6 years old. As an immigrant, I have faced many adversities that have challenged me both emotionally and physically. Looking back, I would not change a single thing. All those past experiences have made me who I am today. There have been countless individuals who have given me opportunities that I could have only dreamed of and guided me along the way. I have always wanted to use what I have been given to make an impact on the world. I never knew how until 4 years ago.

After finishing my undergraduate degree in 2019, I joined the mechanical engineering Master's program. I was drawn to renewable energy and electrification. After looking into prevalent issues in both industries I noticed that batteries were a large bottleneck. It was through Dr. Huazhen Fang's guidance I narrowed my interest to battery modeling. My time in his lab proved to be some of the most challenging. The experiences I have gained and the skills I have developed have helped me become a better engineer and person. I deeply appreciate Dr. Fang's efforts and guidance throughout these years.

Next, I would like to thank my committee members - Dr. Gibum Kwon and Dr. Rajesh Rajamani for their time and efforts. I would also like to thank my friends and lab mates. Some of whom have been encouraging me since my first days of undergraduate school. I would like to thank my partner, Ashley Morton, for her unwavering support throughout this time. I would also like to thank my mentor, Dr. Hari Harikumar, who guided me toward graduate school and his discussions about life and philosophy. I am grateful to my family in India for their continued love and support.

Finally, I would like to thank my parents, Shyla Biju and Biju Thankappan. Words cannot describe how grateful I am for all the sacrifices you have made for me. Thank you Amma and Acha for everything you have done and continue to do. Without you, the person I am today and the life I have had the opportunity to live would remain a dream.

Contents

1 Introduction **1**

1.1 Literature Review 1

1.2 Statement of Contributions 4

1.3 Organization 5

2 Development of the BattX Model **6**

3 Rationale for the BattX Model Design **11**

3.1 Connection between Sub-circuit A and SPMeT 11

3.2 Connection between Sub-circuit B and SPMeT 14

3.3 Connection between Sub-circuit D and SPMeT 16

4 Parameter Identification for the BattX Model **17**

5 Simulation and Experimental Validation of the BattX Model **22**

5.1 Simulation-Based Validation 22

5.1.1 Model Identification 22

5.1.2 Model Testing and Validation 24

5.2 Experimental Valdation 28

5.2.1 Model Identification 28

5.2.2 Model Testing and Validation 33

6 Conclusions **37**

A Derivation of $V_{s,1}$ under Constant Current I **40**

B Derivation of $V_{e,1}$ and $V_{e,3}$ under Constant Current I **43**

List of Figures

1.1 Relations of the BattX model with some existing battery models. The light blue and red arrows represent model simplification; the grey dashed arrows represent comparability. 4

2.1 The BattX model comprising: sub-circuit A to simulate the lithium-ion diffusion in the electrode phase; sub-circuit B to simulate the lithium-ion diffusion in the electrolyte phase; sub-circuit C to simulate heat conduction and convection; and sub-circuit D to simulate the terminal voltage. 7

3.1 Spherical discretization of an electrode particle. 12

3.2 Three regions immersed in the electrolyte. 14

4.1 Flowchart for the multipronged experimental data generation and parameter identification. 21

5.1 Terminal voltage profile under intermittent discharging at 0.5 C to identify Θ_{R_o} and fitting of $R_o(\mathrm{SoC})$ with $\tilde{R}_o$ based on $\hat{\Theta}_{R_o}$ 23

5.2 Terminal voltage fitting under 0.5 C constant-current discharging based on $\hat{\Theta}_{U_s}$ . . 24

5.3 Terminal voltage and temperature fitting under 1.5 C and 2 C constant-current discharging based on $\hat{\Theta}_e$, $\hat{\Theta}_{\mathrm{Th}}$, and $\hat{\Theta}_{\mathrm{Arr}}$ 25

5.4 Voltage prediction by the BattX model versus the benchmark truth at 0.25 C and 3 C constant-current discharge 25

5.5 Voltage and temperature prediction by the BattX model versus the benchmark results for a WLTC cycle 26

5.6 Voltage and surface temperature prediction by the BattX model versus the benchmark results for multiple eVTOL cycles 27
5.7 Experimental setup. Left: the PEC® SBT4050 battery tester; right: the cell placed in an Arbin high-current cylindrical cell holder. 28
5.8 SoC/OCV curve fitting based on $\hat{\Theta}_{U_s}$. 30
5.9 Identification of Θ_{R_o}: (left) terminal voltage profile under intermittent discharging at 0.5 C to identify Θ_{R_o}; (right) fitting of $R_o(\mathrm{SoC})$ with $\tilde{R}_o$ based on $\hat{\Theta}_{R_o}$. 30
5.10 Terminal voltage fitting under 0.5 C constant-current discharging based on $\hat{\Theta}_s$. . . . 31
5.11 Temperature fitting and prediction based on $\hat{\Theta}_{\mathrm{Th}}$. 32
5.12 Terminal voltage fitting under 3 C constant-current discharging based on $\hat{\Theta}_e$. 32
5.13 Voltage prediction for constant-current discharging at 0.5, 1, 4, and 5 C. 34
5.14 BattX versus 2RC Thevenin's under a UDDS load. Row 1: the UDDS-based current load profile; row 2: the actual and predicted voltage; row 3: zoomed (left: 2RC Thevenin's; right: BattX); row 4: the voltage prediction error. 35
5.15 Temperature prediction by the BattX model versus the measurements in the UDDS-based test. 35
5.16 BattX versus 2RC Thevenin's under an eVTOL profile. Row 1: the current load profile; row 2: the actual and predicted voltage; row 3: zoomed (left: 2RC Thevenin's; right: BattX); row 4: the voltage prediction error. 36
5.17 Temperature prediction by the BattX model versus the measurements in the test simulating an eVTOL operation cycle. 36

List of Tables

5.1 Estimation of Θ_s 24

5.2 Estimation of Θ_{Th} 26

5.3 Estimation of Θ_e and Θ_{Arr} 27

5.4 Identification summary for Θ_{R_o}, Θ_s, and Θ_{Th}: initial guesses, bound limits, and final estimates. 31

5.5 Identification summary for Θ_{Arr} and Θ_e: initial guesses, bound limits, and final estimates. 33

Chapter 1

Introduction

Lithium-ion batteries (LiBs) are a key power source for consumer electronics, electrified transportation, smart grids, and renewable energy. Compared with alternative secondary storage sources, they provide a set of outstanding characteristics, including high energy/power density, high nominal voltage, no memory effect, low self-discharge rates, and long cycle life [1–3]. Recent technological advances have further improved their power delivery and cost efficiency for a wider application spectrum. The safe and high-performing operation of LiB systems require advanced battery management, which encompasses a wide range of tasks such as condition monitoring, charging control, cell balancing, and aging diagnostics [4–7]. High-quality dynamic models are fundamental to almost all battery management tasks. While the growing research has led to a variety of useful models, the literature still lacks fast and accurate models for applications involving charging/discharging from low to high current rates. To fill this gap, we propose a first-of-its-kind equivalent circuit model named *BattX* and demonstrate its predictive fidelity over broad C-rate ranges in this thesis.

1.1 Literature Review

Research on LiB dynamic modeling has flourished in the past decades to produce an extensive collection of literature. The mainstream models generally fall into two categories: electrochemical models and equivalent circuit models (ECMs). Electrochemical models explicitly describe electrochemical reactions, transport of lithium ions, and distribution of charge and potential inside a LiB cell. Depending on the need for accuracy, they exist on diverse scales, from atomic/molecular to

species level, and in different dimensions, from 1D to 3D and beyond, and are often coupled with different physical processes, e.g., thermodynamics and stress/strain [8]. Generally, electrochemical models present high mechanistic fidelity as well as high computational complexity. Battery management researchers hence must selectively focus on those that offer a desirable accuracy-computation trade-off, due to practical demands for fast computation. A favorable choice is the pseudo-2D Doyle-Fuller-Newman (DFN) model, which describes the diffusion of lithium ions and charge transfer across the electrodes, electrolyte, and separator of a sandwich cell [9]. The search for more efficient models has led to the single-particle model (SPM), which represents each electrode by a single spherical particle and neglects electrolyte dynamics [10]. The simplification enhances computational efficiency to a great extent but also limits the SPM model to low-to-moderate C-rates (around or less than 1 C). Subsequent studies have emerged to expand the SPM model by adding characterization of a cell's thermal behavior [11, 12], electrolyte dynamics [13–17], stress buildup [17], or degradation [18], to elevate its prediction capability. The literature has also presented a few computational methods to speed up the simulation of the SPM model or its improved versions [19, 20].

ECMs represent another important pathway to modeling LiBs. They are circuit analogs composed of electrical components to simulate a cell's dynamic behavior, capture phenomena in charging/discharging, and track state-of-charge (SoC) and power capability. With simple structures, they are accessible for interpretation, easy to calibrate, and scalable to large LiB systems composed of many cells. Also, they are governed by low-order ordinary differential equations, which allows for very fast computation. These benefits combine to make them popular candidates for real-world battery management systems with limited computing resources [21]. A basic ECM, called the Rint model, cascades an open-circuit voltage (OCV) source with an internal resistor, in which the voltage source is SoC-dependent [22]. The Rint model can be added to a set of serially connected RC pairs to describe the transient behavior in a cell's voltage response, leading to the so-called Thevenin model [1, 23]. Depending on the number of RC pairs used, one can set the model to capture transients at multiple time scales [24]. The literature has presented a few approaches to modify

the Thevenin model for better accuracy. For example, the study in [3, 25] incorporates hysteresis in charging/discharging; in [26–29], different circuit parameters (e.g., the internal resistance) are made dependent on the SoC, temperature, or current loads, and the OCV is parameterized using different function forms for higher fitting accuracy. Even though phenomenological ECMs and electrochemical models were largely two disparate threads of research, a growing number of studies have explored developing ECMs drawing upon electrochemical modeling. The work in [30, 31] proposes the nonlinear double capacitor (NDC) model to approximate the ion diffusion in the electrodes of a cell and characterize the nonlinear voltage behavior simultaneously. This model is interpretable as a reduced-order circuit analog to the SPM, and it is further supplemented in [32] with a data-based voltage hysteresis model to attain better accuracy. The study in [33] derives an ECM using circuit elements to characterize charge transfer and diffusion potentials; the derivation also helps explain some conventional ECMs from an electrochemical perspective. In [34], an ECM is coupled with diffusion dynamics to attain higher prediction accuracy. It is increasingly recognized that we can combine ECMs with machine learning. Such hybird models, by design, utilize data-driven representation to elevate the accuracy of ECMs in presence of biases or uncertainty, as reported in [35–37].

Structural simplicity underlies the wide use of ECMs in battery management but also restricts their accuracy. Most of today's ECMs are accurate enough for only low C-rates, and recent progress has led to ECMs that are provably suitable for about 1 C [30, 31]. However, the literature still faces an absence of ECMs capable of predicting a cell's voltage behavior from low to high C-rate ranges. This gap will pose potential barriers for some emerging battery-powered applications that must operate across wide current ranges. One example is electric vertical take-off and landing (eVTOL), which requires discharging of up to 5 C in the take-off and landing phases and necessitates precise models to fulfill high-stakes safety requirements [38].

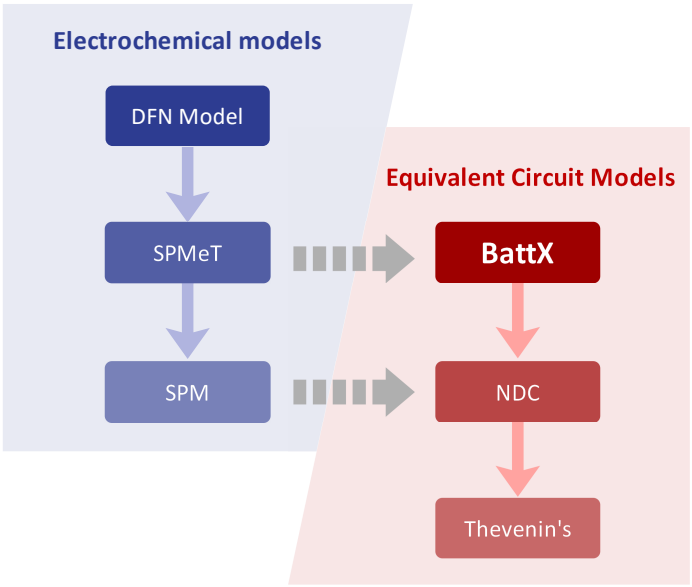

Figure 1.1: Relations of the BattX model with some existing battery models. The light blue and red arrows represent model simplification; the grey dashed arrows represent comparability.

1.2 Statement of Contributions

In this thesis, we present the first ECM designed to predict over broad current ranges. We take inspirations from the SPM with electrolyte and thermal dynamics (SPMeT) to enable the design. Specifically, we propose equivalent circuits to separately simulate a LiB cell's electrode, electrolyte, and thermal dynamics as well as their effects on the terminal voltage, and then conjoin the circuits to set up the ECM. The obtained model, called BattX, comprehensively accounts for different dynamic processes key to a cell's charging/discharging behavior, making it distinct from existing ECMs. This characteristic endows the model with excellent prediction capability from low to high C-rates. The model also retains relatively compact structures to offer high computational efficiency, carrying the potential to facilitate embedded battery management applications. Centering around the BattX model, this paper delivers the following specific contributions.

- We propose the principled design of the BattX model and further elucidate the underlying rationale by showing its connections with the SPMeT model in detail.
- We develop a multipronged parameter identification approach to extract the parameters of

the BattX model from measurement data made on LiBs. This approach can make the model readily available in practice.

- We provide experimental evaluation results to validate the effectiveness and accuracy of the BattX model. The experiments involve charging/discharging across broad C-rate ranges and consider operation profiles of eVOTL as a case study.

Fig. 1.1 further illustrates the connections of the BattX model with some existing models. As is shown, there is a cascade of simplification from the DFN to the SPMeT to the SPM model in the domain of electrochemical models, and the simplification goes from the BattX to the NDC to the Thevenin model in the domain of ECMs. The BattX model is an ECM in form but can be viewed as a circuit analog to the SPMeT model. It thus combines the respective advantages of both types of models to be fast and accurate. Note that the SPMeT model allows for mathematical model order reduction to speed up computation. However, compared to those numerical reduced-order models, the BattX model well lends itself to physical interpretability and experimental calibration.

1.3 Organization

The thesis is based on the research reported in [39, 40], and the rest of it is organized as follows. Chapter 2 presents the BattX model in detail. It is followed by a derivation of the model and a summary of inspirations gained from the SPMeT model in Chapter 3. Chapter 4 develops a parameter identification procedure for the BattX model. Chapter 5 contains the validation via simulation and experiments. Finally, Chapter 6 summarizes the conclusions and the opportunities for future work.

Chapter 2

Development of the BattX Model

This chapter presents the structure and governing equations of the BattX model. The detailed rationale for the model design will be provided in Chapter 3.

At the core, the BattX model attempts to characterize the multiple major dynamic processes innate to a LiB cell in order to capture the cell's behavior from low to high current rates. This is akin to electrochemical modeling to a certain extent, but the main difference is that the BattX model leverages circuit analogs to simulate the processes. Fig. 2.1 shows the overarching structure of the model. As shown, it consists of four coupled sub-circuits, which are labeled A to D. These sub-circuits are designed to approximate the cell's electrode-phase diffusion, electrolyte-phase diffusion, thermal evolution, and voltage response, respectively.

To begin with, sub-circuit A uses a chain of resistors and capacitors to approximate lithium-ion diffusion in the electrode phase. Its governing equations are

$$\dot{V}_{s,1}(t) = \frac{V_{s,2}(t) - V_{s,1}(t)}{C_{s,1}R_{s,1}} + \frac{I(t)}{C_{s,1}}, \tag{2.1a}$$

$$\dot{V}_{s,i}(t) = \frac{V_{s,i-1}(t) - V_{s,i}(t)}{C_{s,i}R_{s,i-1}} + \frac{V_{s,i+1}(t) - V_{s,i}(t)}{C_{s,i}R_{s,i}}, \quad i = 2, \ldots, N-1 \tag{2.1b}$$

$$\dot{V}_{s,N}(t) = \frac{V_{s,N-1}(t) - V_{s,N}(t)}{C_{s,N}R_{s,N-1}}, \tag{2.1c}$$

where I is the applied current, with $I > 0$ for charging and $I < 0$ for discharging, $V_{s,j}$ for $j = 1, \ldots, N$ are the voltages across the individual capacitors $C_{s,j}$, $R_{s,j}$ are the resistors that the current must flow through, and the subscript s indicates solid phase. We set $0 \leq V_{s,j} \leq 1$ for the purpose of normalization and then define the SoC as the percentage ratio of the currently available

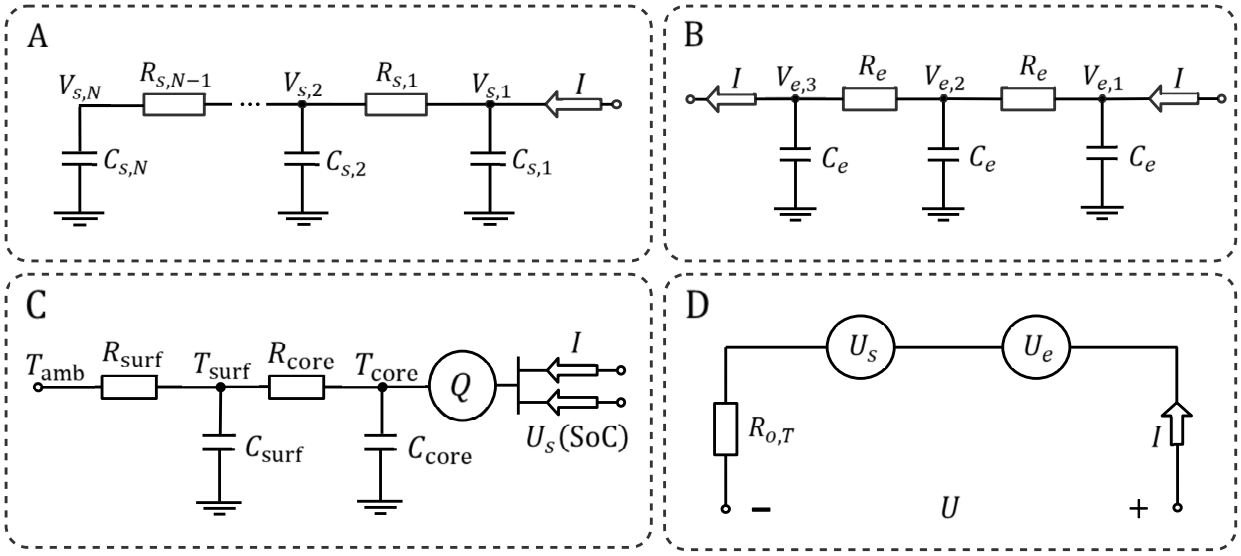

Figure 2.1: The BattX model comprising: sub-circuit A to simulate the lithium-ion diffusion in the electrode phase; sub-circuit B to simulate the lithium-ion diffusion in the electrolyte phase; sub-circuit C to simulate heat conduction and convection; and sub-circuit D to simulate the terminal voltage.

charge over the total charge capacity, which is

$$\text{SoC} = \frac{\sum_{j=1}^{N} C_{s,j} V_{s,j}}{\sum_{j=1}^{N} C_{s,j}} \times 100\%.$$

That is, $\text{SoC} = 100\%$ when $V_{s,j} = 1$ for all j, and $\text{SoC} = 0$ when $V_{s,j} = 0$ for all j. A brief interpretation of sub-circuit A is as follows, with more details to be shown in Chapter 3. Overall, the charge transfer between the capacitors in the circuit mimics the diffusion of lithium ions in the solid phase or electrode. Then, $V_{s,j}$ for $j = 1, \ldots, N$ correspond to the lithium-ion concentrations at N different locations, from the surface to the center, that spread along the radius of an electrode sphere; $C_{s,j}$ for $j = 1, \ldots, N$ are analogous to the volumes of the subdomains if one subdivides the electrode sphere at these discrete locations; $R_{s,j}$ for $j = 1, \ldots, N-1$ resist the charge transfer or equivalently, the solid-phase diffusion in the SPMeT model, and are hence inversely proportional to the diffusivity.

Along similar lines to sub-circuit A, sub-circuit B uses a resistor-capacitor chain to approximate

the diffusion of lithium-ions in the electrolyte. Its dynamics are governed by

$$\dot{V}_{e,1}(t) = \frac{V_{e,2}(t) - V_{e,1}(t)}{C_e R_e} + \frac{I(t)}{C_e}, \tag{2.2a}$$

$$\dot{V}_{e,2}(t) = \frac{V_{e,1}(t) - 2V_{e,2}(t) + V_{e,3}(t)}{C_e R_e}, \tag{2.2b}$$

$$\dot{V}_{e,3}(t) = \frac{V_{e,2}(t) - V_{e,3}(t)}{C_e R_e} - \frac{I(t)}{C_e}, \tag{2.2c}$$

where the notations above have similar meanings as in (2.1), and the subscript e refers to the electrolyte. We let $0 \leq V_{e,j} \leq 1$ for $j = 1, 2, 3$ as in the case of $V_{s,j}$, and further assume that $V_{e,j} = 0.5$ for $j = 1, 2, 3$ when the cell is at equilibrium. One can interpret sub-circuit B as analogous to the one-dimensional electrolyte-phase diffusion being discretized along the spatial coordinate. In particular, $V_{e,j}$ for $j = 1, 2, 3$ can be associated with the lithium-ion concentrations at the locations of the anode, separator, and cathode, and R_e embodies resistance to diffusion in the electrolyte. The spatial discretization is assumed to be uniform, thus leading to the same values of R_e and C_e for each region as shown in (2.2).

Sub-circuit C is a lumped circuit model for the thermal dynamics, with the design inspired by [41]. Here, we consider the cell to be cylindrical without loss of generality and concentrate its spatial dimensions into two singular points that represent the surface and core, respectively. This simplification allows us to describe the evolution of the temperatures at these two points, T_{surf} and T_{core}, by

$$\dot{T}_{\text{core}}(t) = \frac{Q(t)}{C_{\text{core}}} + \frac{T_{\text{surf}}(t) - T_{\text{core}}(t)}{R_{\text{core}} C_{\text{core}}}, \tag{2.3a}$$

$$\dot{T}_{\text{surf}}(t) = \frac{T_{\text{amb}}(t) - T_{\text{surf}}(t)}{R_{\text{surf}} C_{\text{surf}}} - \frac{T_{\text{surf}}(t) - T_{\text{core}}(t)}{R_{\text{core}} C_{\text{surf}}}, \tag{2.3b}$$

where T_{amb} is the ambient temperature, $C_{\text{surf/core}}$ and $R_{\text{surf/core}}$ represents the thermal capacitance and resistance at the surface and core, respectively, and Q is the internal heat generation rate accompanying electrochemical reactions inside the cell during charging/discharging. From a heat transfer perspective, (2.3a) approximately describes the heat conduction between the cell's surface

and core, and (2.3b) grasps the convection between the surface and the ambient environment. Further, Q is characterized as

$$Q = -I\left[U_s\left(\mathrm{SOC}\right) - U_s(V_{s,1}) - R_{o,T}I\right], \tag{2.4}$$

where $U_s(\cdot)$ is the nonlinear OCV function, $V_{s,1}$ is defined in sub-circuit A, and $R_{o,T}$ is the internal resistance. $R_{o,T}$ is not a constant and instead depends on SoC and T_{core} to capture the polarization resistance. It is given by

$$R_{o,T} = R_o(\mathrm{SoC}) \cdot \exp\left(\kappa_1\left(\frac{1}{T_{\mathrm{core}}} - \frac{1}{T_{\mathrm{amb}}}\right)\right), \tag{2.5}$$

where κ_1 is a constant coefficient. In the equation above, the first term $R_o(\mathrm{SoC})$ captures the dependence of $R_{o,T}$ on $V_{s,1}$ and takes the form

$$R_o(\mathrm{SoC}) = \gamma_1 + \gamma_2 \cdot \exp\left(-\gamma_3 \mathrm{SoC}\right), \tag{2.6}$$

where γ_i for $i = 1, 2, 3$ are coefficients, and the second term shows the temperature dependence due to the Arrhenius law. Similarly, an Arrhenius relationship can be used to capture the relationship between the electrode-phase diffusion constant and temperature:

$$R_{s,1,T} = R_{s,1} \cdot \exp\left(\kappa_2\left(\frac{1}{T_{\mathrm{core}}} - \frac{1}{T_{\mathrm{amb}}}\right)\right). \tag{2.7}$$

Finally, sub-circuit D summarizes the effects of the solid-phase and electrolyte-phase dynamics on the terminal voltage. It contains two voltage sources, U_s and U_e, in series with an internal resistance $R_{o,T}$. The terminal voltage, U, is given by

$$U = U_s(V_{s,1}(t)) + U_e(V_{e,1}(t), V_{e,N_e}(t)) + R_{o,T}I(t). \tag{2.8}$$

Here, U_s simulates the solid-phase OCV. As the SPMeT model mandates that the open-circuit

potential of solid material relies on the lithium-ion concentration at the surface of the electrode, U_s should come as a function of $V_{s,1}$, and its exact form will depend on the cell. Next, we need to determine the form of U_e. In the SPMeT model, the electrolyte potential depends on the electrolyte concentration at the anode and cathode. We hence make U_e as a function of $V_{e,1}$ and V_{e,N_e} and express it as

$$U_e(t) = \beta_1 \left(\ln \left(\frac{V_{e,1}(t) + \beta_2}{V_{e,3}(t) + \beta_2} \right) \right), \tag{2.9}$$

where β_i for $i = 1, 2$ are constant coefficients. Putting together all the above equations, we will obtain a complete description of the BattX model. This model is the first ECM that can predict over broad current ranges, due to the integration of the circuits approximating the electrode, electrolyte, and thermal dynamics into a whole. The model design also leads to profound comparability with electrochemical modeling, especially the SPMeT, which will be revealed further in the next chapter. We will address the identification of the model parameters in Chapter 4.

Chapter 3

Rationale for the BattX Model Design

In this chapter, we will draw on the SPMeT model to explain the rationale for the design of the BattX model. We will show that the SPMeT model if appropriately discretized, will reduce to a structure that is approximately equivalent to the proposed circuit analogs of the BattX model. Our main references about the SPMeT model include [14, 16, 42]. We will focus on expounding sub-circuits A, B, and D, with the sub-circuit C-based lumped thermal model well addressed in [41].

3.1 Connection between Sub-circuit A and SPMeT

The SPMeT model characteristically couples the SPM model with the electrolyte and thermal dynamics. What it inherits from the SPM model is the representation of the electrodes as two spherical particles. The diffusion of lithium-ions in each particle follows Fick's second law in spherical coordinates [11, 12]:

$$\frac{\partial c_{s,j}(r,t)}{\partial t} = \frac{D_{s,j}}{r^2}\frac{\partial}{\partial r}\left(r^2\frac{\partial c_{s,j}(r,t)}{\partial r}\right), \tag{3.1}$$

where $c_{s,j}$ is the solid-phase (electrode) lithium-ion concentration, D_s is the constant diffusion coefficient, and r is the radial coordinate. The subscript $j \in \{n, p\}$, where n and p refer to the anode (negative) and cathode (positive), respectively. The boundary conditions for (3.1) are

$$\left.\frac{\mathrm{d}c_{s,j}}{\mathrm{d}r}\right|_{r=0} = 0, \quad \left.\frac{\mathrm{d}c_{s,j}}{\mathrm{d}r}\right|_{r=R_j} = -\frac{J_j}{D_{s,j}},$$

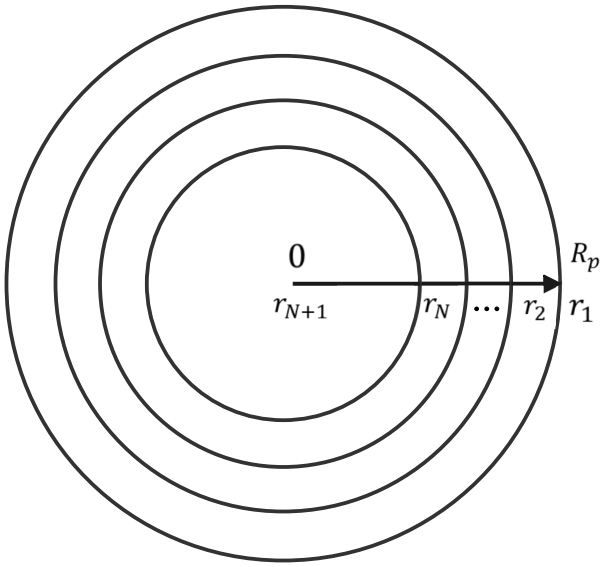

Figure 3.1: Spherical discretization of an electrode particle.

where R is the radius of a particle. The molar flux J at the electrode/electrolyte interface is given by

$$J_p(t) = \frac{i(t)}{FS_p}, \quad J_n(t) = -\frac{i(t)}{FS_n},$$

where i is the applied current density, with $i > 0$ for charging and $i < 0$ for discharging, S is the surface area of a particle, and F is Faraday's constant.

Next, let us reduce the PDE in (3.1) into a system of ODE equations using a finite volume method [43, 44]. The subscript $j \in n, p$ will be dropped in sequel without causing confusion. First, we subdivide the particle into a set of continuous finite volumes at discrete locations $r_1 = R > r_2 > \ldots > r_N > r_{N+1} = 0$ that spreads inward from the surface to the center, as show in Fig. 3.1. The amount of lithium-ions within the ith finite volume is given by

$$Q_i(t) = \int_{r_{i+1}}^{r_i} c_s(r,t) dV = \int_{r_{i+1}}^{r_i} c_s(r,t) \cdot 4\pi r^2 dr,$$

for $i = 1, \ldots, N$. Then, using (3.1), we have

$$\begin{aligned} \dot{Q}_i(t) = \int_{r_{i+1}}^{r_i} \dot{c}_s(r,t) \cdot 4\pi r^2 dr = \\ \int_{r_{i+1}}^{r_i} d\left(4\pi D_s r^2 \frac{\partial c_s(r,t)}{\partial r}\right) = \\ 4\pi D_s r_i^2 \left.\frac{\partial c_s(r,t)}{\partial r}\right|_{r_i} - 4\pi D_s r_{i+1}^2 \left.\frac{\partial c_s(r,t)}{\partial r}\right|_{r_{i+1}}. \end{aligned} \tag{3.2}$$

To proceed, we replace $c_s(r,t)$ by the average lithium-ion concentration within the ith finite volume, $\bar{c}_s(r_i,t)$:

$$\bar{c}_s(r_i,t) = \frac{Q_i(t)}{\Delta V_i}, \tag{3.3}$$

where $\Delta V_i = 4\pi(r_i^3 - r_{i+1}^3)/3$. From (3.2)-(3.3), it follows that

$$\dot{\bar{c}}_s(r,t) = \frac{4\pi D_s r_i^2}{\Delta V_i} \left.\frac{\partial c_s(r,t)}{\partial r}\right|_{r_i} - \frac{4\pi D_s r_{i+1}^2}{\Delta V_i} \left.\frac{\partial c_s(r,t)}{\partial r}\right|_{r_{i+1}}.$$

Then, we approximate the concentration gradient along the radial coordinate as

$$\left.\frac{\partial c_s(r,t)}{\partial r}\right|_{r_i} = \frac{\bar{c}(r_{i-1},t) - \bar{c}(r_i,t)}{\Delta r_i},$$

where $\Delta r_i = (r_{i-1} - r_{i+1})/2$. Given the boundary conditions, we further have

$$\dot{\bar{c}}_s(r_1,t) = -\frac{4\pi D_s r_2^2}{\Delta V_1 \Delta r_2}\left(\bar{c}_s(r_1,t) - \bar{c}_s(r_2,t)\right) + \frac{4\pi r_1^2}{\Delta V_1 F S} i(t), \tag{3.4a}$$

$$\dot{\bar{c}}_s(r_i,t) = \frac{4\pi D_s r_i^2}{\Delta V_i \Delta r_i}\left(\bar{c}_s(r_{i-1},t) - \bar{c}_s(r_i,t)\right) - \frac{4\pi D_s r_{i+1}^2}{\Delta V_i \Delta r_{i+1}}\left(\bar{c}_s(r_i,t) - \bar{c}_s(r_{i+1},t)\right), \tag{3.4b}$$

$$\dot{\bar{c}}_s(r_N,t) = \frac{4\pi D_s r_N^2}{\Delta V_N \Delta r_N}\left(\bar{c}_s(r_{N-1},t) - \bar{c}_s(r_N,t)\right). \tag{3.4c}$$

for $i = 2, \ldots, N-1$. The above ODEs show the spatially discretized solid-phase diffusion. Note that they share the same structure with (2.1). A closer inspection of (2.1) and (3.4) suggests: 1)

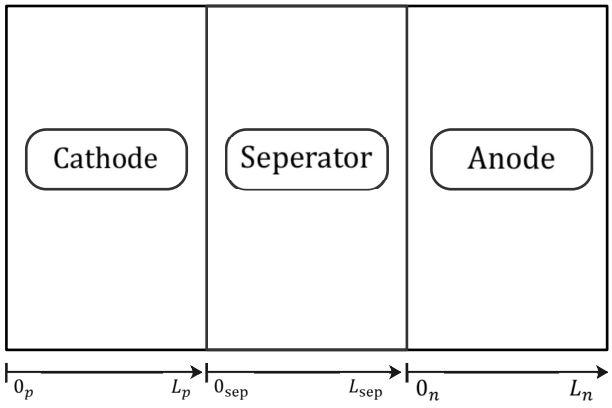

Figure 3.2: Three regions immersed in the electrolyte.

V_s is a mirror of $\bar{c}_s(r,t)$, and its distribution reflects the distribution of lithium-ion concentrations inside an electrode particle; 2) C_s is a mirror of ΔV, associating the capacitance with the volume of a finite volume element within the particle; 3) R_s roughly corresponds to $\Delta r/(D_s \cdot 4\pi r^2)$ to grasp the effect of D_s, Δr and r on the diffusion resistance at different locations. This unveiled connection with the SPMeT model justifies the design of sub-circuit A.

3.2 Connection between Sub-circuit B and SPMeT

The SPMeT model includes one-dimensional electrolyte diffusion, which also follows Fick's second law. Electrolyte diffusion is considered in the electrode and separator domains that are all immersed in the electrolyte. Based on the coordinates in each domain as shown in Fig. 3.2, the governing equations are

$$\frac{\partial c_{e,p}(x,t)}{\partial t} = D_e \frac{\partial^2 c_{e,p}(x,t)}{\partial x^2} + \frac{1-t_c^0}{\epsilon_{e,p} F L_p} i(t), \tag{3.5a}$$

$$\frac{\partial c_{e,\text{sep}}(x,t)}{\partial t} = D_e \frac{\partial^2 c_{e,\text{sep}}(x,t)}{\partial x^2}, \tag{3.5b}$$

$$\frac{\partial c_{e,n}(x,t)}{\partial t} = D_e \frac{\partial^2 c_{e,n}(x,t)}{\partial x^2} - \frac{1-t_c^0}{\epsilon_{e,n} F L_n} i(t), \tag{3.5c}$$

where $c_{e,j}$ for $j \in \{n, p, \text{sep}\}$ is the lithium-ion concentration in the electrolyte surrounding the anode, cathode and separator, $\epsilon_{e,j}$ is the electrolyte volume fraction, $D_{e,j}$ is the electrolyte diffusion

coefficient, and t_c^0 is the constant transference number. We assume that $\epsilon_{e,j}$ and $D_{e,j}$ are the same for any $j \in \{n, p, \text{sep}\}$. The boundary conditions are given by

$$\begin{aligned}
\frac{\partial c_{e,p}(0_p, t)}{\partial x} &= \frac{\partial c_{e,n}(L_n, t)}{\partial x} = 0, \\
\frac{\partial c_{e,p}(L_p, t)}{\partial x} &= \frac{\partial c_{e,\text{sep}}(0_{\text{sep}}, t)}{\partial x}, \\
\frac{\partial c_{e,\text{sep}}(L_{\text{sep}}, t)}{\partial x} &= \frac{\partial c_{e,n}(0_n, t)}{\partial x}, \\
c_e(L_p, t) &= c_e(0_{\text{sep}}, t), \\
c_e(L_{\text{sep}}, t) &= c_e(L_n, t).
\end{aligned}$$

To convert (3.5) into ODEs, we concentrate the electrodes and separator into singular points and further suppose $L_p = L_n$ and L_{sep} is negligible. The singular point that represents the electrodes are located at the midpoint of each domain, and the average lithium-ion concentration is denoted as $\bar{c}_{e,j}$. Then, we apply the finite difference method to (3.5) and obtain

$$\dot{\bar{c}}_{e,p}(t) = \frac{4D_e}{L^2}\left(\bar{c}_{e,\text{sep}}(t) - \bar{c}_{e,p}(t)\right) + \frac{1 - t_c^0}{\epsilon_e F L} i(t), \tag{3.6a}$$

$$\dot{\bar{c}}_{e,\text{sep}}(t) = \frac{4D_e}{L^2}\left(\bar{c}_{e,p}(t) - 2\bar{c}_{e,\text{sep}}(t) + \bar{c}_{e,n}(t)\right), \tag{3.6b}$$

$$\dot{\bar{c}}_{e,n}(t) = \frac{4D_e}{L^2}\left(\bar{c}_{e,\text{sep}}(t) - \bar{c}_{e,n}(t)\right) - \frac{1 - t_c^0}{\epsilon_e F L} i(t). \tag{3.6c}$$

As is seen, (3.5) is structurally similar to (2.2), and the similarity lends to the interpretation of (2.2) through the lens of electrochemical modeling. Specifically, we can associate $V_{e,1}$, $V_{e,2}$ and $V_{e,3}$ with $\bar{c}_{e,p}$, $\bar{c}_{e,\text{sep}}$, and $\bar{c}_{e,n}$, respectively. Further, C_e can be linked with the spatial lengths of the electrode domains, which decide the volume of the electrolyte, and R_e comes as the inverse of D_e to measure the resistance against electrolyte diffusion.

3.3 Connection between Sub-circuit D and SPMeT

In the SPMeT model, the terminal voltage V consists of four terms that represent the solid-phase OCV, electrolyte-phase voltage, overpotential, and voltage over the film resistance, respectively. Then, coming back to sub-circuit D of the BattX model, U_s mirrors the solid-phase OCV, U_e corresponds to the electrolyte-phase voltage, and $R_{o,T}$ plays a role to mainly capture the film resistance as well as the overpotential effect. Less trivially, we elaborate on the form of U_e in (2.9). The electrolyte-phase voltage is given by

$$\phi_e(0_p, t) - \phi_e(L_n, t) = \frac{L_p + 2L_{sep} + L_n}{2\bar{k}} i(t) + k_{\text{conc}} \left(\ln c_e(0_p, t) - \ln c_e(L_n, t) \right), \tag{3.7}$$

where ϕ_e is the electrolyte electric potential, and $\bar{k}$ and k_{conc} are two coefficients that are related to electrolyte conductivity and molar activity. The first term above is accounted for through $R_{o,T}$. Following the discussion in Chapter 3.2, we can approximate the second term as

$$k_{\text{conc}} \left(\ln \bar{c}_{e,p}(t) - \ln \bar{c}_{e,n}(t) \right).$$

This form is found to bear equivalence to (2.9), when making linear projections of $\bar{c}_{e,p}(t)$ and $\bar{c}_{e,n}(t)$ to $V_{e,1}$ and $V_{e,3}$, respectively.

Chapter 4

Parameter Identification for the BattX Model

In this chapter, we investigate how to determine the parameters of the BattX model. To this end, we separate the model's parameters into different groups based on the dynamic processes that they belong to or prominently influence. We then design experiments accordingly and use different current profiles to excite different dynamic processes and obtain voltage or temperature data suitable for the identification of the corresponding parameter groups. Finally, we extract the parameters from the data, group by group, through data fitting and some empirical tuning.

To begin with, we set up the following parameter groups for the BattX model:

- $\Theta_{U_s} = \{\alpha_i, i = 0, 1, \ldots, 16\}$, which includes the parameters in U_s in sub-circuit D;
- $\Theta_{R_o} = \{\gamma_i, i = 1, 2, 3\}$, which includes the parameters in R_o in sub-circuit D;
- $\Theta_s = \{C_{s,i}, i = 1, \ldots, N, R_{s,j}, j = 1, \ldots, N-1\}$, which includes the parameters of sub-circuit A;
- $\Theta_{\mathrm{Th}} = \{C_{\mathrm{surf}}, R_{\mathrm{surf}}, C_{\mathrm{core}}, R_{\mathrm{core}}\}$, which includes the parameters in the lumped thermal model in sub-circuit C;
- $\Theta_e = \{C_e, R_e, \beta_1, \beta_2\}$, which includes the parameters in sub-circuit B and the parameters in U_e in sub-circuit D;
- $\Theta_{\mathrm{Arr}} = \{\kappa_1, \kappa_2\}$, which includes the Arrhenius-law-related parameters;.

By grouping the parameters as above, we can design different current input profiles to stimulate different parts of the cell's dynamics so as to identify the parameters group by group. This multi-pronged approach includes the following steps.

Step 1: Identification of Θ_{U_s}. Since U_s represents the OCV source, we can capture it by applying a trickle constant current with a magnitude of $1/30$ C to fully charge or discharge the cell. As the current is extremely small, sub-circuit A, which is an analog to the solid (electrode)-phase diffusion, is almost always at equilibrium, with $V_{s_i} = \mathrm{SoC}$ for $i = 1, \ldots, N$ (SoC can be obtained via Coulomb counting); meanwhile, sub-circuits B and C, U_e, and the voltage across $R_{o,T}$, are all negligible in this case. Hence, $U \approx U_s$, and we can construct the following data fitting problem to identify Θ_{U_s}:

$$\hat{\Theta}_{U_s} = \arg\min_{\Theta_{U_s}} \sum_{t_k} \left[U(t_k) - U_s\left(\mathrm{SoC}(t_k); \Theta_{U_s}\right)\right]^2, \tag{4.1}$$

where k is the discrete time index in the experiment.

Step 2: Identification of Θ_{R_o}. R_o is an integral part of the internal resistance $R_{o,T}$, and $R_o = R_{o,T}$ when $T = T_{\mathrm{ref}}$. To identify Θ_{R_o}, we apply a 0.5 C pulse current profile, which includes long enough rest periods between two consecutive pulses to allow for sufficient voltage recovery, to discharge the cell from 100% to 0% of SoC when the ambient temperature is T_{ref}. With discharging at 0.5 C, the cell will only see a negligible increase in its temperature, and $U_e \approx 0$. For the terminal voltage U, we will see a sharp drop or jump at the beginning or end of every pulse, and this is almost solely due to the voltage change across R_o. Therefore, using the voltage jump, one can approximate R_o as

$$\tilde{R}_o(t_*) = \left|\frac{U(t_{*+1}) - U(t_*)}{I}\right|, \tag{4.2}$$

where t_* is the instant when a pulse stops. Further, the instantaneous SoC can be readily determined via Coulomb counting. Collecting R_o for all t_*, we can formulate the following data fitting problem to estimate Θ_{R_o}:

$$\hat{\Theta}_{R_o} = \arg\min_{\Theta_{R_o}} \sum_{t_*} \left[\tilde{R}_o(t_*) - R_o(\Theta_{R_o}; t_*)\right]^2. \tag{4.3}$$

Step 3: Identification of Θ_s. The number of parameters in Θ_s depends on N, and when N is large, Θ_s will be poorly identifiable to defy accurate estimation. To formulate a tractable identification problem, we assume that

$$C_{s,i} = \eta_i C_{s,1},\ R_{s,j} = \sigma_j R_{s,1}, \tag{4.4}$$

where η_i and σ_i for $i = 1, \dots N$ and $j = 1, \dots N-1$ are pre-specified coefficients with $\eta_1 = \sigma_1 = 1$, and $\sum_{i=1}^{N} \eta_i C_{s,i}$ is the total capacity of the cell. This allows us to consider only two parameters, i.e., $\Theta_s = \{C_{s,1}, R_{s,1}\}$, greatly facilitating the parameter estimation. The simplification is also reasonable—the difference among $C_{s,i}$ and $R_{s,j}$ can be viewed as a result of the selection of the discretization points as shown in (3.4), and one can specify η_i and σ_j assuming that they result from a certain selection. The practical selection of η_i and σ_j can be done through an analysis of the discretization shown in Chapter 3.1 and tuning. Going forward, we apply a 0.5 C constant-current profile to discharge the cell from full to zero SoC. In this setting, sub-circuit A is excited, but the dynamics of sub-circuits B and C have no appreciable effects. That is, the cell's temperature remains almost the same, and $U_e \approx 0$. We can conduct data fitting as below to find out Θ_s:

$$\hat{\Theta}_s = \arg\min_{\Theta_s} \sum_{t_k} \left[U(t_k) - R_o\left(\hat{\Theta}_{R_o}; t_k\right) I(t_k) - U_s\left(V_{s,1}\left(\Theta_s; t_k\right); \hat{\Theta}_{U_s}\right)\right]^2, \tag{4.5}$$

where $\hat{\Theta}_{U_s}$ and $\hat{\Theta}_{R_o}$ have been obtained in Steps 1 and 2, and the form of $V_{s,1}(\Theta_s, t)$ is derived in Appendix.A.

Step 4: Identification of Θ_{Th}. Based on [41], a straightforward idea to determine Θ_{Th} is to fit it to the measurement data of T_{surf} and/or T_{core} given the lumped thermal model in (2.3). However, the idea is hard to be applied here, because Q in our model is dependent on $R_{o,T}$, as shown in (2.4), and unavailable before $R_{o,T}$ is identified. To overcome this issue, we choose to use prior knowledge to guide the estimation of Θ_{Th}. Here, we can approximate R_{core} based on the conductivity of the cell's electrode materials and jellyroll structure. Furthermore, we can infer R_{surf} and C_{surf} from the form factors and specifications, casing material (usually aluminum), and the cooling

system. Finally, C_{core} can be deduced given the cell's total heat capacity. A 2C constant current full discharge profile is used to acquire the data encompassing significant temperature changes. With the measurement data, we can begin from the approximate values of the parameters and continually tune them until achieving sufficient fitting accuracy to finalize $\hat{\Theta}_{\text{Th}}$.

Step 5: Identification of Θ_e and Θ_{Arr}. Sub-circuit B will have substantial effects on U only at high C-rates. Therefore, we use a 3 C constant current profile to fully discharge the cell such that large enough U_e will result and present itself into the voltage response. This then allows to identify Θ_e. In the meantime, 3 C discharging will subject the cell to important temperature increases, which, in turn, will drive down Θ_{Arr}-dependent $R_{s,T}$ and $R_{o,T}$ and influence the voltage response. As such, we need to consider the estimation of Θ_e and Θ_{Arr} together. The following data fitting problem can be formulated:

$$\begin{aligned}\hat{\Theta}_{\text{e}}, \hat{\Theta}_{\text{Arr}} = \arg \min_{\Theta_{\text{e}}, \Theta_{\text{Arr}}} \sum_{t_k} [U(t_k) - R_{o,T}\left(\hat{\Theta}_{R_o}, \Theta_{\text{Arr}}, T_{t_k}; t_k\right) I(t_k) \\ -U_s\left(V_{s,1}\left(\hat{\Theta}_s, \Theta_{\text{Arr}}, T_{t_k}; t_k\right); \hat{\Theta}_{U_s}\right) - U_e\left(\Theta_e; t_k\right)]^2.\end{aligned} \tag{4.6}$$

Here, U_e depends on $V_{e,1}$ and $V_{e,3}$ as shown in (2.9), and the explicit form of $V_{e,1}$ and $V_{e,3}$ is shown in Appendix.B. Note that no closed-form expression of U_s exists in this step, as the changing $R_{s,T}$ makes sub-circuit A become a time-varying system. It is thus impossible to solve the problem in (4.6) using nonlinear optimization. To alleviate the difficulty, we suggest to apply some empirical tuning. Specifically, we can pick a sample of Θ_{Arr} using prior knowledge, then estimate Θ_e by solving the above data fitting problem, and iterate this procedure until getting the lowest possible fitting errors. Despite the time and effort needed, this iterative method is often found effective with a sufficient number of tries.

The above steps together constitute our parameter identification approach for the BattX model and are summarized in the flowchart in Fig. 4.1. The following remarks summarize our further insights.

Remark 1 *We point out that the data fitting problems outlined in Steps 1-5 are non-trivial to solve,*

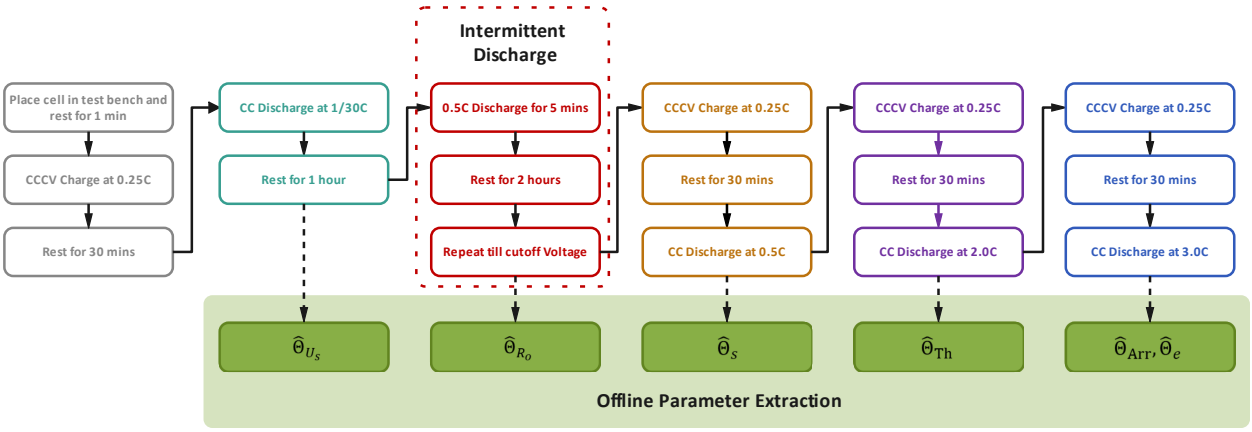

Figure 4.1: Flowchart for the multipronged experimental data generation and parameter identification.

as they entail nonlinear nonconvex optimization. The nonconvexity can easily get the parameter search stuck in local minima to produce physically meaningless parameter estimates. To mitigate the issue, it is sensible to constrain the search within a believably correct parameter space [24]. Specifically, one can set up approximate lower and upper bounds for every possible parameter and then limit the numerical optimization within the resultant parameter space. The prior knowledge used to establish such bounds can be derived from both experience and observation or analysis of the measurement data. Other helpful ways to overcome the local minima issue include adding regularization terms that encode prior knowledge of some parameters and applying different initial guesses to repeatedly run the numerical optimization [24].

Remark 2 *We consider Samsung INR18650-25R cells (see Chapter 5.2 for the specifications) as a baseline when selecting the discharging C-rates in each step of the above approach, because they are used in the experimental validation of the BattX model (see Chapter 5.2). However, a user or practitioner may need to adjust the specific C-rates, depending on the cells to apply the model. The overall guiding rule is the same—using current profiles of different C-rates to excite different dynamic processes to obtain data informative for the identification of the parameters associated with each process.*

Chapter 5

Simulation and Experimental Validation of the BattX Model

This chapter presents the simulation and experimental validations of the model. Both sets of validation will include model identification followed by validation.

5.1 Simulation-Based Validation

All simulations are carried out using GT-SUITE Version 2023, a multi-physics systems simulation platform [45]. GT-SUITE executes a pseudo-two-dimensional electrochemical model through the GT-AutoLion template. We set the electrochemical model to simulate an NMC811 energy-dense pouch cell with a nominal capacity of 18 Ah and run it to generate synthetic datasets. We then calibrate the BattX model using the datasets and compare its prediction performance relative to the electrochemical model.

5.1.1 Model Identification

The OCV-SOC relationship was directly extracted from the AutoLion1D model and used in U_s as a lookup table, thus, eliminating the need to find $\hat{\Theta}_{U_s}$. The identification then follows the steps highlighted in Fig. 4.1.

- First, the electrochemical model was run with a 0.5 C pulse load profile shown in Fig. 5.1. The voltage from the simulation was used to calculate R_o using (4.2) and then (4.3) to find $\hat{\Theta}_{R_o}$. The calibrated $\hat{R}_o$ is given by

$$\hat{R}_o = -0.0383V_{s1}^3 + 0.0875V_{s,1}^2 - 0.0655V_{s,1} + 0.0226.$$

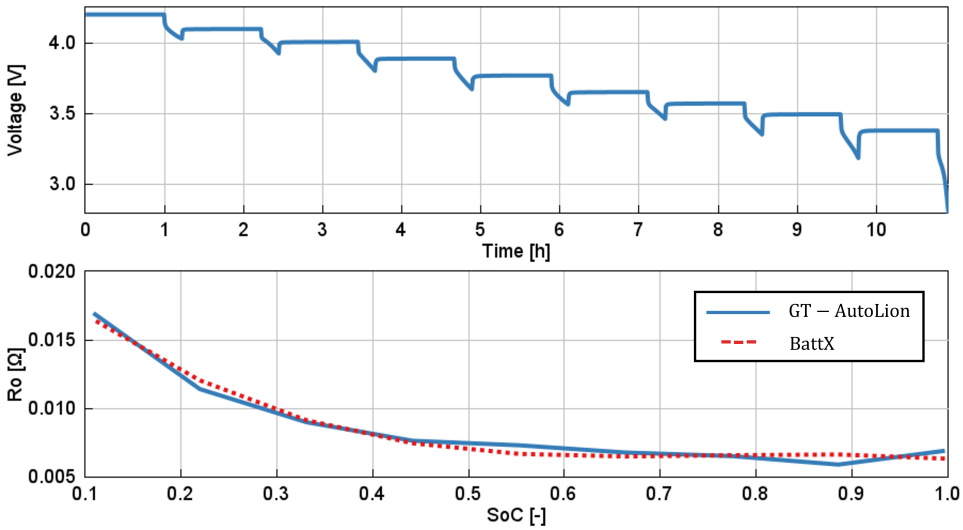

Figure 5.1: Terminal voltage profile under intermittent discharging at 0.5 C to identify Θ_{R_o} and fitting of $R_o(\mathrm{SoC})$ with $\tilde{R}_o$ based on $\hat{\Theta}_{R_o}$

Fig. 5.1 compares $\hat{R}_o$ with the benchmark truth, showing satisfactory accuracy.

- Next, the OCV-SOC relationship from the electrochemical model was transferred into the BattX table in a table lookup format. Then, using some knowledge of the electrochemical model and of the spatial discretization, we can specify

$$\eta_i = \{1, 0.6066, 0.3115, 0.1148, 0.0164\}\,,$$
$$\sigma_j = \{1, 1.77, 4.00, 15.98\}\,.$$

  Then, a 0.5 C constant-current discharge was applied to the electrochemical model. The voltage output from the simulation was used to identify $\hat{\Theta}_s$. The identified parameters are summarized in Table 5.1, and the comparison between the predicted terminal voltage and the benchmark is shown in Fig. 5.2.

- Finally, the electrochemical model was simulated under 1.5 C and 2 C constant-current discharge loads separately. The voltage and average temperature data from the simulation were used to identify $\hat{\Theta}_{\mathrm{Th}}, \hat{\Theta}_e$, and $\hat{\Theta}_{\mathrm{Arr}}$. The optimal parameters are summarized in Tables 5.2

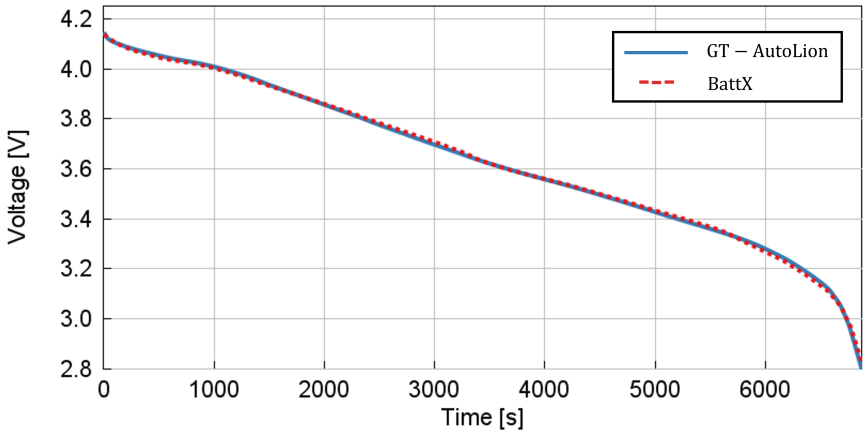

Figure 5.2: Terminal voltage fitting under 0.5 C constant-current discharging based on $\hat{\Theta}_{U_s}$

and 5.3 with the prediction results shown in Fig. 5.3.

The above summarizes the identification of the BattX model using AutoLion1D. Next, we apply the identified model to new datasets to further validate it.

5.1.2 Model Testing and Validation

To test the predictive capability of the calibrated BattX model, we generated new datasets based on the electrochemical model. The first tests assess the model using low and high constant current discharge profiles. Fig. 5.4 shows the voltage prediction at 0.25 C and 3 C constant-current discharge. It is seen that the BattX model can deliver good accuracy in both cases.

The next dataset was generated based on a profile from the Worldwide harmonized Light vehicles Test Cycles (WLTC), which are real-world dynamometer tests by light-duty vehicles. Here,

Table 5.1: Estimation of Θ_s

	$C_{s,1}$	$R_{s,1}$
Initial Guess	33316	0.07
Lower Bound	30000	0.01
Upper Bound	35000	0.15
Optimal Value	33124	0.02

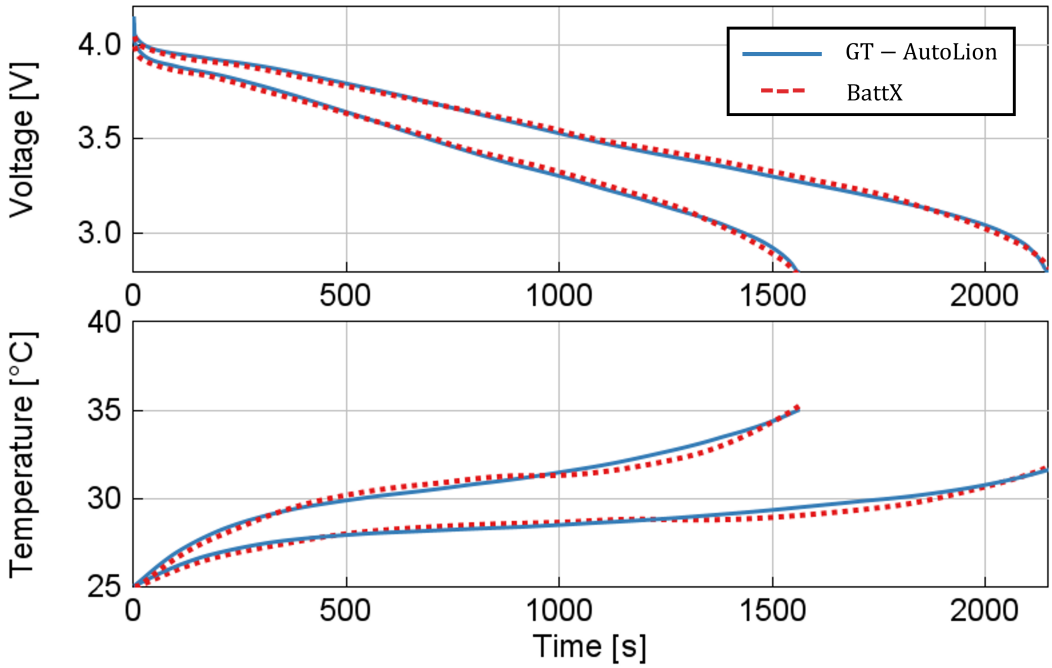

Figure 5.3: Terminal voltage and temperature fitting under 1.5 C and 2 C constant-current discharging based on $\hat{\Theta}_e$, $\hat{\Theta}_{\text{Th}}$, and $\hat{\Theta}_{\text{Arr}}$

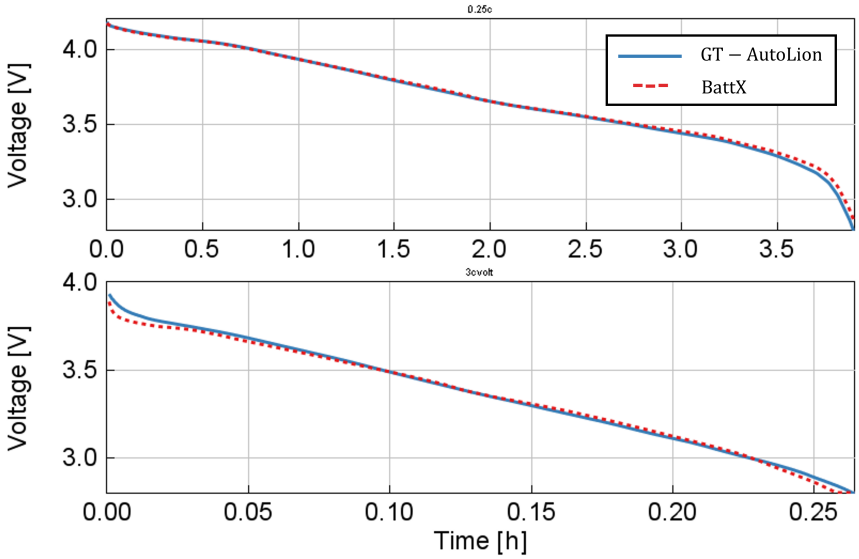

Figure 5.4: Voltage prediction by the BattX model versus the benchmark truth at 0.25 C and 3 C constant-current discharge

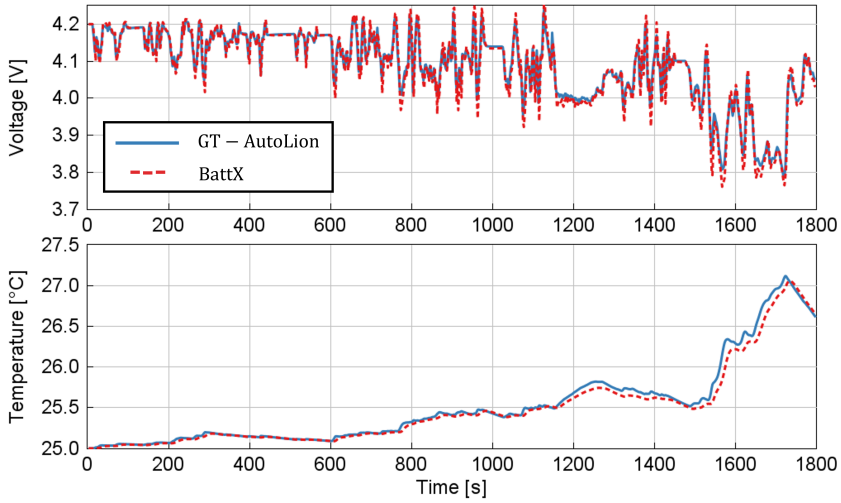

Figure 5.5: Voltage and temperature prediction by the BattX model versus the benchmark results for a WLTC cycle

we normalized the power loads to be appropriate for the cell, supplying the cell with currents varying from -2 to 3 C. The voltage and temperature prediction by the BattX model are shown in Fig. 5.5, showing excellent agreement with the benchmark.

The third dataset was intended for LiB-powered eVTOL. Although eVTOL has attracted increasing interest as a promising solution to urban air mobility and decarbonization of aviation, conventional ECMs are hardly suitable for them, because they require high-rate discharging in the takeoff and landing phases [38]. The proposed BattX model holds a promise to overcome the issue. We consider a notional eVTOL flight here, which includes three phases, takeoff, cruising, and landing. The three phases are assumed to require discharging at 2.8 C, 0.8 C, and 2.8 C. The

Table 5.2: Estimation of Θ_{Th}

	R_{surf}	R_{core}	C_{surf}	C_{core}
Initial Guess	0.65	0.25	120	250
Lower Bound	0.59	0.10	100	180
Upper Bound	0.75	0.50	150	320
Optimal Value	0.71	0.12	117	189

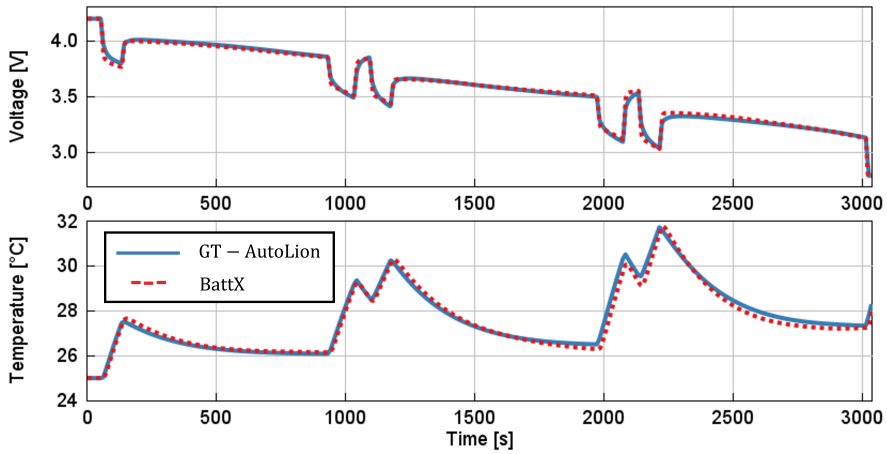

Figure 5.6: Voltage and surface temperature prediction by the BattX model versus the benchmark results for multiple eVTOL cycles

corresponding discharging power for the considered cell is 54 W, 16 W, and 54 W, respectively. Accordingly, we generated a current load profile sequentially comprising multiple flight cycles with the three-phase pattern until the cell reaches its cutoff voltage. Fig. 5.6 shows that the BattX model achieves accurate prediction compared with the benchmark truth. Especially, the accuracy is found satisfactory at the times of high discharge rates. The surface temperature prediction in Fig. 5.6 also well agrees with the actual temperature.

To sum up, the testing and validation results show the high accuracy and fidelity of the BattX model across low to high currents in different use scenarios. Next, we present the validation results using experimental data.

Table 5.3: Estimation of Θ_e and Θ_{Arr}

	β_0	R_e	C_e	κ_1	κ_2
Initial Guess	1.2	45000	1e-4	18	40
Lower Bound	0.9	35000	8.0e-5	15.0	10.0
Upper Bound	2.0	70000	1.2e-4	22.0	50.0
Optimal Value	1.9	53088	8.6e-5	21.6	27.1

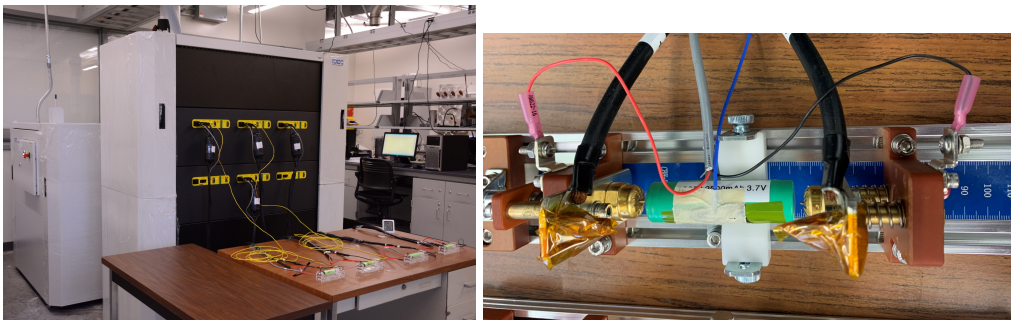

Figure 5.7: Experimental setup. Left: the PEC® SBT4050 battery tester; right: the cell placed in an Arbin high-current cylindrical cell holder.

5.2 Experimental Valdation

All the experiments were conducted on a Samsung INR18650-25R cell with NCA cathode and graphite anode using a PEC® SBT4050 battery tester and placed in an Arbin cylindrical cell holder, as shown in Fig. 5.7. The cell's nominal capacity is 2.5 Ah, nominal voltage is 3.6 V, maximum cut-off voltage is 4.2 V, minimum cut-off voltage is 2.5 V, and maximum continuous discharge current is 20 A. The tester is able to run charging or discharging tests of up to 40 V and 50 A under arbitrary current or power load profiles. The cell holder is capable of testing high-capacity 18650 cells at up to 200 A.

Similar to to the simulation validation, the experiment is comprised of two parts. The first part collected datasets following the parameter identification approach in Chapter 4 to identify the model parameters. In the second part, new datasets were generated to evaluate the predictive capability and computational cost of the identified model against the Thevenin model.

5.2.1 Model Identification

The experiments and model identification procedure is as follows.

- Based on Chapter 4, we first charged the cell using the popular constant-current/constant-voltage method, let it rest for one hour, and then fully discharged it using a 1/30 C constant-current load. We calculated the total capacity to be 2.55 Ah using the Coulomb counting

method and then intended to use the voltage data to find $\hat{\Theta}_{U_s}$. The following non-linear function was used to predict the OCV of the cell:

$$U_s(V_{s,1}) = h_1\left(V_{s,1}\right) \cdot H\left(0.9 - V_{s,1}\right) + h_2\left(V_{s,1}\right) \cdot H\left(V_{s,1} - 0.9\right),$$

where $H(\cdot)$ is the Heaviside step function, $h_1(V_{s,1})$ captures the behavior when $V_{s,1} \leq 0.9$ as

$$\begin{aligned} h_1(V_{s,1}) = \alpha_0 + \alpha_1 \frac{1}{1+\exp(\alpha_2(V_{s,1}(t) - \alpha_3))} + \\ \alpha_4 \frac{1}{1+\exp(\alpha_5(V_{s,1} - \alpha_6))} + \\ \alpha_7 \frac{1}{1+\exp(\alpha_8(V_{s,1} - \alpha_9))} + \\ \alpha_{10} \frac{1}{1+\exp(\alpha_{11} V_{s,1}(t))} + \alpha_{12} V_{s,1}(t), \end{aligned}$$

and $h_2(V_{s,1})$ is for when $0.9 < V_{s,1} \leq 1$ with

$$h_2(V_{s,1}) = \alpha_{13}\exp(\alpha_{14} V_{s,1}) + \alpha_{15}\exp(\alpha_{16} V_{s,1}).$$

Here, α_i for $i = 0, \ldots, 15$ are constant coefficients. Then, $\hat{\Theta}_{U_s}$ was found based on (4.1):

$$\begin{aligned} \hat{\Theta}_{U_s} = \{&-9.048, -2.360, -12.986, 0.010, 13.036, -32.840, -0.087, 2.359, \\ &-14.863, 0.055, -0.788, -7.136, 0.966, 31.132, -3.414, 0.513, 1.816\}. \end{aligned}$$

The SoC/OCV fitting result under the obtained $\hat{\Theta}_{U_s}$ is shown in Fig. 5.8.

- Next, the cell was charged to full again, idled for one hour, and then discharged under a 0.5 C pulse load profile. Specifically, a load was applied for five minutes, followed by a one-hour rest, and this cycle continued until the cut-off voltage was met. Fig. 5.9 shows the profile, which includes a total of 12 pulses. With the data, we calculated R_o at different SoC via (4.2) and then used (4.3) to compute $\hat{\Theta}_{R_o}$ as shown in Table 5.4. The reconstructed R_o is

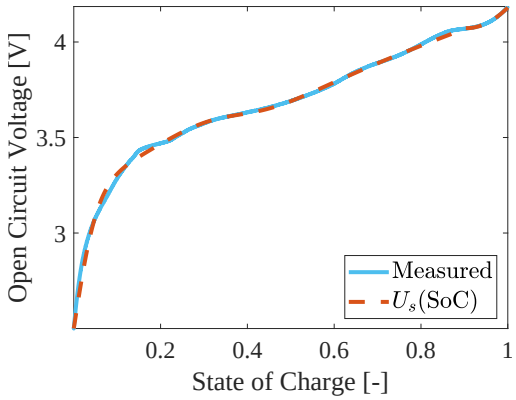

Figure 5.8: SoC/OCV curve fitting based on $\hat{\Theta}_{U_s}$.

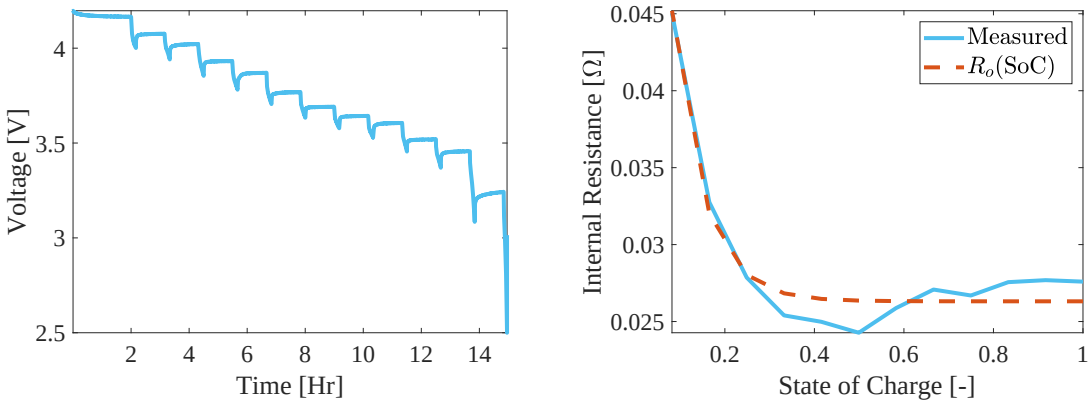

Figure 5.9: Identification of Θ_{R_o}: (left) terminal voltage profile under intermittent discharging at 0.5 C to identify Θ_{R_o}; (right) fitting of $R_o(\mathrm{SoC})$ with $\tilde{R}_o$ based on $\hat{\Theta}_{R_o}$.

compared with the measurements in Fig. 5.9.

- Going further, we fully charged the cell again as in the previous steps, and then fully discharged it using a 0.5 C constant-current load, with the objective of identifying Θ_s. As explained in Chapter 4, we could impose a pre-determined relation like (4.4) to reduce the number of parameters to estimate. Here, we let the spherical particle be discretized into five finite volumes, and the resulting η_i and σ_j are

$$\eta_i = \{1, 0.6066, 0.3115, 0.1148, 0.0164\}\,,$$

$$\sigma_j = \{1, 1.77, 4.00, 15.98\}\,.$$

Table 5.4: Identification summary for Θ_{R_o}, Θ_s, and Θ_{Th}: initial guesses, bound limits, and final estimates.

Name	γ_1	γ_2	γ_3	$C_{s,1}$	$R_{s,1}$	C_{surf}	R_{surf}	C_{core}	R_{core}
Initial Guess	1	1	1	4391	0.090	7	6	20	1
Lower Bound	-	-	-	3600	0.054	3	3	5	0.5
Upper Bound	-	-	-	5500	0.167	12	20	50	7
Final estimate	0.026	0.061	14.36	4521	0.114	10	7	40	4

Fig. 5.10 illustrates a comparison between the predicted terminal voltage (with the dynamics of sub-circuits B and C neglected) based on $\hat{\Theta}_s$ and the measurements. Table 5.4 shows the estimation for $\hat{\Theta}_s$.

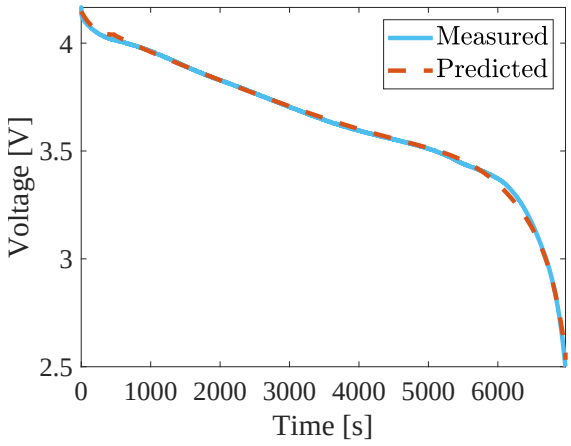

Figure 5.10: Terminal voltage fitting under 0.5 C constant-current discharging based on $\hat{\Theta}_s$.

- Then, we ran a 2 C constant-current discharging test to collect the temperature data. The cell's surface temperature increased by about 10 K throughout the test. We leveraged prior knowledge and empirical tuning to determine Θ_{Th}, as suggested in Chapter 4. While the procedure is coarse-grained, we obtained $\hat{\Theta}_{\text{Th}}$ that leads to accurate fitting with the surface temperature data and physically reasonable estimation of the core temperature, as shown in Fig. 5.11. Table 5.4 summarizes the numerical estimates of $\hat{\Theta}_{\text{Th}}$.

- Finally, the cell was fully discharged at a constant current of 3 C to excite the cell's electrolyte dynamic and thermal behavior more discernible, for the purpose of identifying Θ_e and

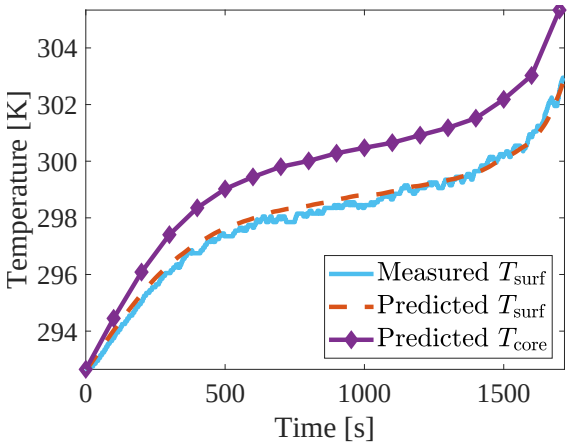

Figure 5.11: Temperature fitting and prediction based on $\hat{\Theta}_{\text{Th}}$.

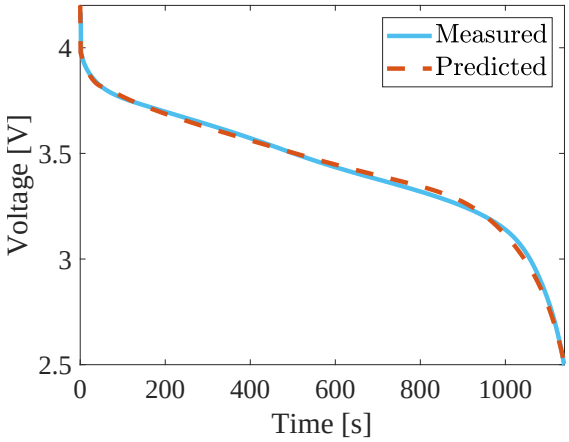

Figure 5.12: Terminal voltage fitting under 3 C constant-current discharging based on $\hat{\Theta}_e$.

Θ_{Arr}. Following Chapter 4, we iteratively tuned $\hat{\Theta}_{\text{Arr}}$ and then ran (4.6) to find $\hat{\Theta}_e$ until the achievement of both physically sound estimates and accurate voltage data fitting. Fig. 5.12 shows that the BattX model based on all the identified parameters fits well the measured voltage, and Table 5.5 shows the estimation results.

From above, we have come up with an explicit setup of the BattX model for the cell. Next, we will fit the model to new datasets to assess how well it predicts.

Table 5.5: Identification summary for Θ_{Arr} and Θ_e: initial guesses, bound limits, and final estimates.

Name	C_e	R_e	β_1	β_2	κ_1	κ_2
Initial Guess	1032	0.028	0.53	0.31	15	22
Lower Bound	500	0.002	0.42	0.19	10	10
Upper Bound	5000	0.080	1.00	0.423	100	100
Final estimate	3691	0.007	0.789	0.317	30	70

5.2.2 Model Testing and Validation

To further evaluate the obtained BattX model, we generated new datasets by applying a variety of load profiles that span a range of currents. The first tests involved fully discharging the cell at a constant current of 0.5, 1, 4, and 5 C separately. Fig. 5.13 compares the BattX model's prediction of the terminal voltage against the measurement, where a close match is observed in all four cases. Note that, even though the model was identified based on tests of only up to 3 C, it can well predict 4 C and 5 C, suggesting its high fidelity.

Further, we adopted the Urban Dynamometer Driving Schedule (UDDS) as a variable load profile and scaled it to be between -8 C and 5 C to validate the BattX model. Here, we desire to compare the BattX model against the popular Thevenin model with two RC pairs. To calibrate the 2RC Thevenin model, we utilize the same nonlinear OCV relationship shown in Fig. 5.8 and then use the 1 C constant-current discharging data to determine all its RC parameters. The validation result is shown in Fig. 5.14. The top figure in Fig. 5.14 illustrates the load profile, which includes both charging and discharging as well as a rest period. The voltage prediction of the BattX model, as shown in Fig. 5.14, closely follows the true voltage overall. A slight discrepancy appears at the end of the test when the cell is about to be depleted. This is likely because the radical changes of the internal resistance at low SoC and high temperature are hard to be thoroughly captured. By contrast, the 2RC Thevenin's model gives a poor prediction, especially when the current load is above 1 C. Fig. 5.15 then demonstrates the comparison of the predicted surface temperature by the BattX model with the measurement, showing an acceptable accuracy. The estimation of

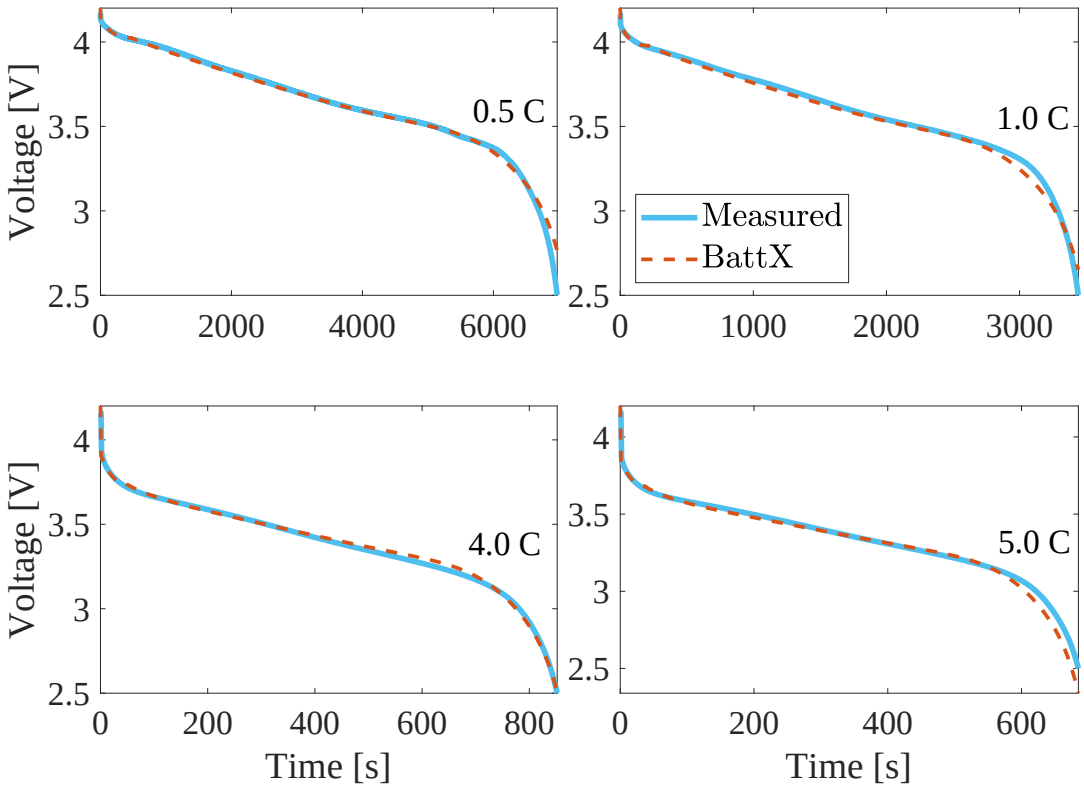

Figure 5.13: Voltage prediction for constant-current discharging at 0.5, 1, 4, and 5 C.

the core temperature is also given in Fig. 5.15, which is reasonable by empirical knowledge and observation.

Similar to Chapter 5.1, we consider a notional eVTOL flight, which includes three phases, takeoff, cruising, and landing [38]. We generated a current load profile sequentially comprising a flight, full discharge, and another flight. Fig. 5.16 displays the current load profile over time and the voltage prediction by the BattX model and by the 2RC Thevenin model. It is seen that the BattX model achieves accurate prediction compared with the measurement. Especially, the accuracy is found satisfactory at times of high discharge rates. The 2RC Thevenin's model, however, generates considerably larger prediction errors and finds itself struggling to capture the cell's voltage behavior at high C-rates. These error magnitudes render the model far from sufficient for the eVTOL application. For the BattX model, the surface temperature prediction in Fig. 5.17 also well agrees with the actual temperature, and the core temperature estimation shows a real trend that one

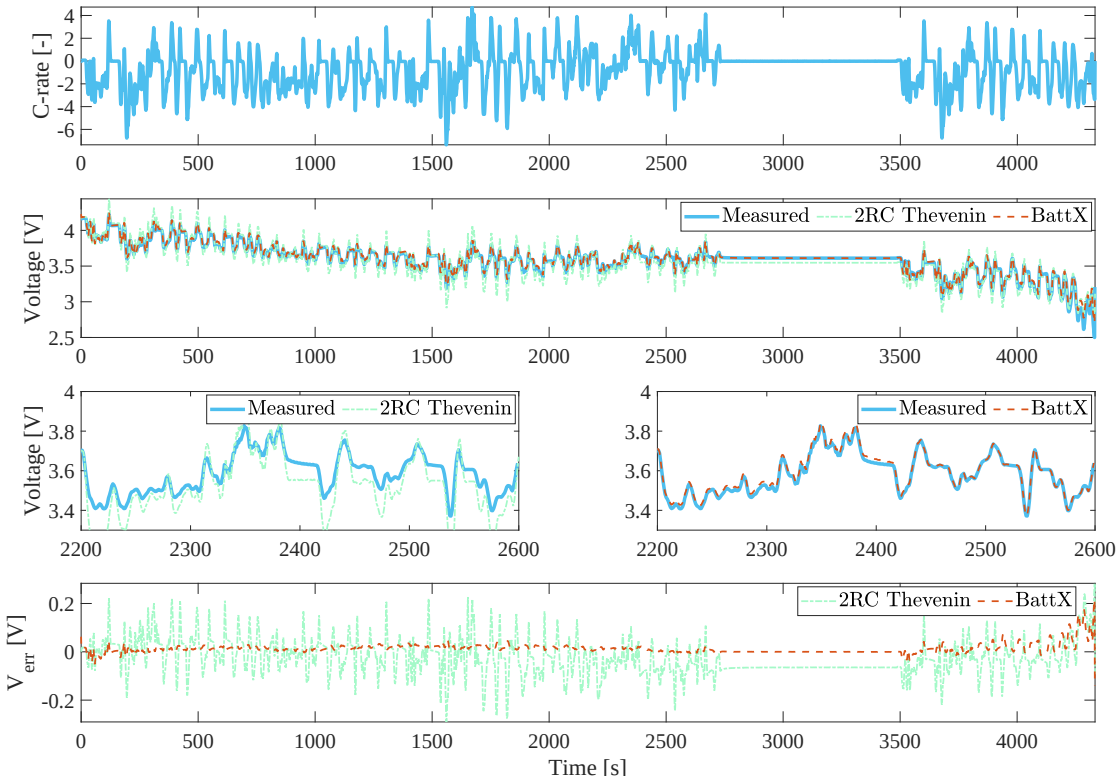

Figure 5.14: BattX versus 2RC Thevenin's under a UDDS load. Row 1: the UDDS-based current load profile; row 2: the actual and predicted voltage; row 3: zoomed (left: 2RC Thevenin's; right: BattX); row 4: the voltage prediction error.

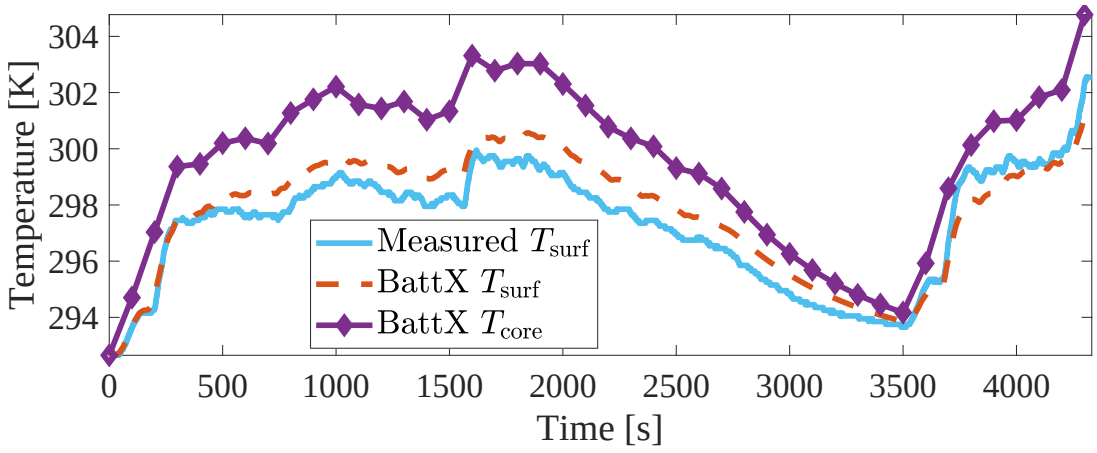

Figure 5.15: Temperature prediction by the BattX model versus the measurements in the UDDS-based test.

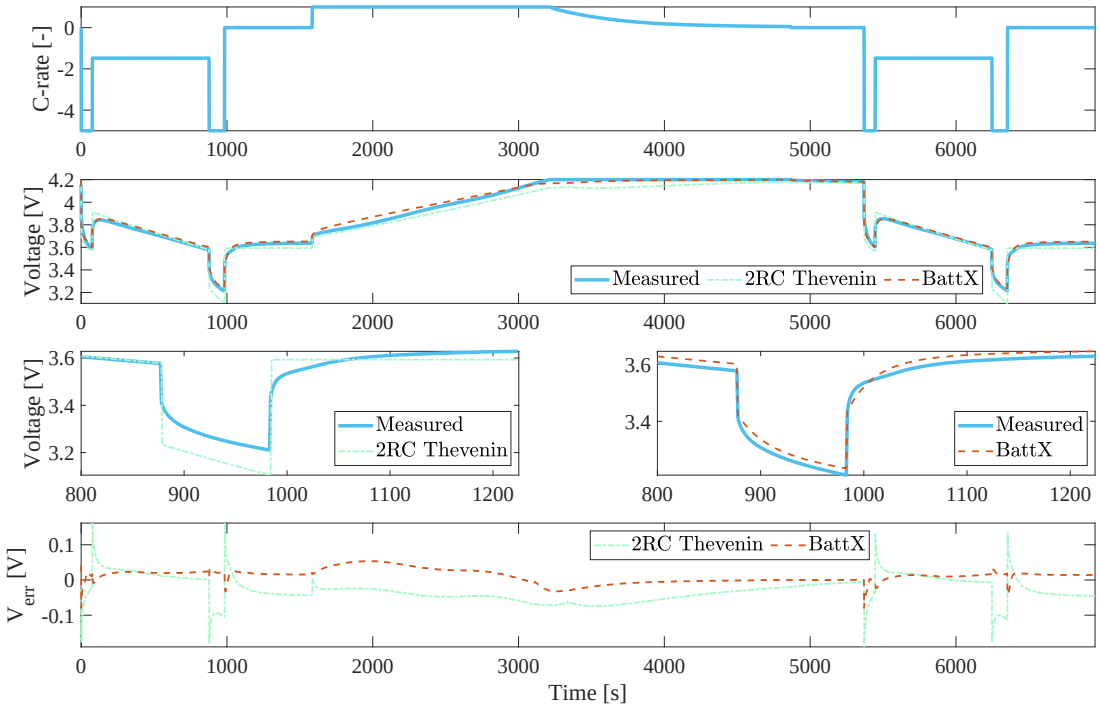

Figure 5.16: BattX versus 2RC Thevenin's under an eVTOL profile. Row 1: the current load profile; row 2: the actual and predicted voltage; row 3: zoomed (left: 2RC Thevenin's; right: BattX); row 4: the voltage prediction error.

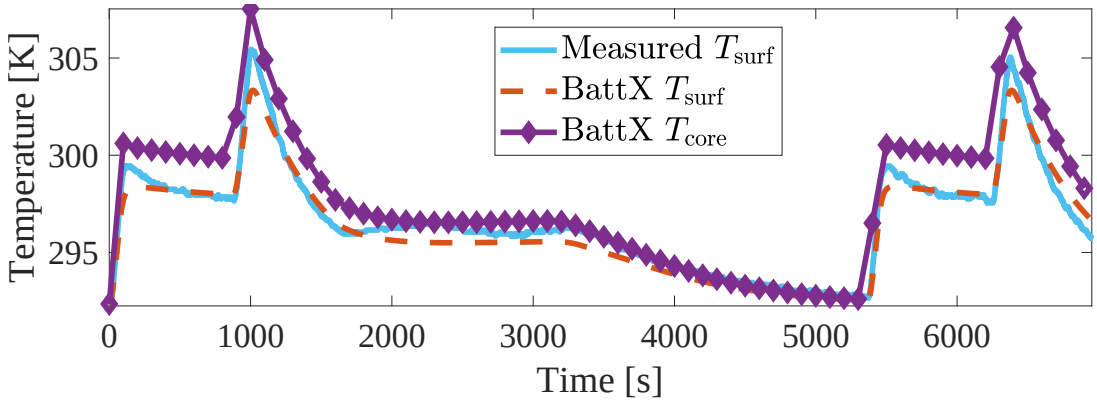

Figure 5.17: Temperature prediction by the BattX model versus the measurements in the test simulating an eVTOL operation cycle.

can trust to be close enough to the truth.

Chapter 6

Conclusions

LiBs have found their way into many sectors as a key technology to drive forward electrification and decarbonization. For LiB applications, computationally fast and accurate ECMs are a bedrock for real-time monitoring and simulation to ensure their performance and safety. Although the literature has presented several different ECMs, none of them is effective when current loads range from low to high. To overcome the problem, we proposed the BattX model in this thesis. This model is an ECM in its form, but unlike other ECMs, it lends to interpretation as a quasi-electrochemical model. This is because it is designed to use separate yet coupled circuits to approximate the lithium-ion diffusion in the electrode and electrolyte phases, heat transfer, and nonlinear voltage behavior in charging/discharging of a cell. With this novel design, the model offers high predictive accuracy over broad current ranges and still retains relatively simple structures for low computational costs. We also developed a parameter identification approach for the model. The approach groups the parameters based on the dynamic processes or components that they belong to and then identifies the parameters of each group using experimental data. Finally, the simulation and experimental validation showed that the BattX model has high accuracy and fidelity across low to high C-rates.

While our study proposed and validated the BattX model, there is still an abundance of opportunities to further improve it or build new study based on it as our future work. Specifically, we can deal with the following aspects.

- *Internal Resistance:* In its present form, the BattX model considers SoC- and temperature-dependent internal resistance. It will be worthy to add the dependence on the C-rate to the

characterization of the internal resistance, as many LiB cells exhibit this feature.

- *Heat Generation:* A LiB cell has four different sources of internal heat generation: resistive heat dissipation, reversible entropic heat, heat produced or consumed through chemical reactions, and heat produced due to the formation and relaxation of concentration gradients within the cell [46]. The BattX model only captures the resistive dissipation, because the last two terms can be assumed to be negligible for cylindrical cells. However, the reversible entropic heat generation becomes more prevalent for certain chemistries, such as LFP [46, 47]. We can enhance the model accounting for this phenomenon.

- *Hysteresis:* A LiB cell's OCV can be different depending on the direction of the current, which is known as *hysteresis*. A common practice is to take the average of the OCV during discharge and charge to find the true OCV of the cell. The BattX model determines $\hat{\Theta}_{U_s}$ by fitting to the average OCV data. We believe that the voltage prediction can be further improved by adding a hysteresis term to the BattX model.

- *Degradation:* A LiB cell will experience capacity and power fade, as a result of complex degradation mechanisms, including SEI growth, active material isolation, or lithium plating. Degradation is a slow process but still critically affects the model accuracy. Currently, the BattX model needs to be re-calibrated to address degradation-caused parameter changes. It will be interesting and useful to improve the model such that it is able to handle the effects of degradation throughout the cell's clycle life.

- *SoC estimation:* It is a non-trivial task to estimate the SOC of a cell. This is especially true for the BattX model, because its complexity is higher than other ECMs to a certain extent. In order to accurately predict SoC using the model, nonlinear estimation techniques will be needed, and it is an open question to make an effective design.

In summary, the BattX model proposed in this thesis advances the state of the art in battery modeling, with potential use in a wide array of applications. The presented study will also open

subsequent research pursuits to further improve the model and leverage it to enable different battery management tasks.

Appendix A

Derivation of $V_{s,1}$ under Constant Current I

In Chapter 4, the identification of Θ_s in (4.5) requires the expression of $V_{s,1}$ when the applied current I is constant. The derivation is as follows.

Consider the governing equations of sub-circuit A in (2.1) under the assumption in (4.4), and rewrite them compactly into the following form:

$$\dot{V}_s(t) = A_s V_s(t) + B_s I(t), \tag{A.1}$$

where

$$\begin{aligned}
V_s &= \begin{bmatrix} V_{s,1} & V_{s,2} & \cdots & V_{s,N} \end{bmatrix}^\top, \\
A_s &= \mu_s \Omega_s, \\
\mu_s &= \frac{1}{C_{s,1} R_{s,1}}, \\
\Omega_s &= \begin{bmatrix}
\frac{-1}{\eta_1 \sigma_1} & \frac{1}{\eta_1 \sigma_1} & 0 & \cdots & \cdots & 0 \\
\frac{1}{\eta_2 \sigma_1} & -\frac{1}{\eta_2 \sigma_1} - \frac{1}{\eta_2 \sigma_2} & \frac{1}{\eta_2 \sigma_2} & 0 & \cdots & 0 \\
\vdots & \vdots & \vdots & \ddots & \ddots & \vdots \\
0 & \cdots & \cdots & 0 & \frac{1}{\eta_N \sigma_{N-1}} & \frac{-1}{\eta_N \sigma_{N-1}}
\end{bmatrix}, \\
B_s &= \begin{bmatrix} \frac{1}{C_{s,1}} & 0 & \cdots & 0 \end{bmatrix}^\top.
\end{aligned}$$

The solution to (A.1) is given by

$$V_s(t) = e^{A_s t} V_s(0) + \int_0^t e^{A_s(t-\tau)} B_s I(\tau) d\tau.$$

When I is constant, it becomes

$$V_s(t) = e^{A_s t} V_s(0) + \int_0^t e^{A_s(t-\tau)} d\tau \cdot B_s I. \tag{A.2}$$

To find the explicit form of $V_s(t)$, we must derive the expression of $e^{A_s t}$. To this end, we look at Ω_s first and note that it is rank-deficient with one zero eigenvalue. Further, assume the other non-zero eigenvalues to be distinct, and denote the eigenvalues of Ω_s as λ_i for $i = 1, 2, \ldots, N$ with $\lambda_1 = 0$. Then, by the Cayley-Hamilton theorem, we have

$$e^{A_s t} = \left[\Phi^{-1} \phi(\mu_s, t)\right] \otimes \Omega_s, \tag{A.3}$$

where

$$\Phi = \begin{bmatrix} 1 & \lambda_1 & \cdots & \lambda_1^{N-1} \\ 1 & \lambda_2 & \cdots & \lambda_2^{N-1} \\ \vdots & \vdots & \ddots & \vdots \\ 1 & \lambda_N & \cdots & \lambda_N^{N-1} \end{bmatrix},$$

$$\phi(\mu_s, t) = \begin{bmatrix} 1 & e^{\mu_s \lambda_2 t} & \cdots & e^{\mu_s \lambda_N t} \end{bmatrix}^\top.$$

The operator $\otimes$ is defined as

$$a \otimes A = \sum_{i=1}^{n} a_i A^{i-1},$$

for $a \in \mathbb{R}^{n\times 1}$ and $A \in \mathbb{R}^{n\times n}$. Inserting (A.3) into (B.2), we obtain

$$\begin{aligned} V_s(t) &= \left[\Phi^{-1}\phi(\mu_s,t)\right] \otimes \Omega_s \cdot V_s(0) + \int_0^t \left[\Phi^{-1}\phi(\mu_s,t-\tau)\right] \otimes \Omega_s d\tau \cdot B_s I \\ &= \left[\Phi^{-1}\phi(\mu_s,t)\right] \otimes \Omega_s \cdot V_s(0) + \left[\Phi^{-1}\int_0^t \phi(\mu_s,t-\tau)d\tau\right] \otimes \Omega_s \cdot B_s I \\ &= \left[\Phi^{-1}\phi(\mu_s,t)\right] \otimes \Omega_s \cdot V_s(0) + \left[\Phi^{-1}\left(\bar{\phi}(\mu_s,t) - \bar{\phi}(\mu_s,0)\right)\right] \otimes \Omega_s \cdot B_s I, \end{aligned} \tag{A.4}$$

where

$$\bar{\phi}(\mu_s,t) = \begin{bmatrix} t & \frac{e^{\mu_s\lambda_2 t}}{\mu_s\lambda_2} & \cdots & \frac{e^{\mu_s\lambda_N t}}{\mu_s\lambda_N} \end{bmatrix}^\top.$$

Given (A.4), $V_{s,1}$ can be expressed as

$$V_{s,1}(t) = \mathbf{e}_1^\top V_s(t),$$

where $\mathbf{e}_1 = \begin{bmatrix} 1 & 0 & \cdots & 0 \end{bmatrix}^\top_{N\times 1}$.

Appendix B

Derivation of $V_{e,1}$ and $V_{e,3}$ under Constant Current I

The explicit expressions of $V_{e,1}$ and $V_{e,3}$ under a constant current I are needed to represent U_e for the identification of Θ_e in (4.6). We can follow similar lines in Appendix.A to find them out. Let us rewrite the governing equations of sub-circuit B in (2.2) compactly as

$$\dot{V}_e(t) = A_e V_e(t) + B_e I(t), \tag{B.1}$$

where

$$\begin{aligned}
V_e &= \begin{bmatrix} V_{e,1} & V_{s,2} & V_{e,3} \end{bmatrix}^\top, \\
A_e &= \mu_e \Omega_e, \\
\mu_e &= \frac{1}{C_e R_e}, \\
\Omega_e &= \begin{bmatrix} -1 & 1 & 0 \\ 1 & -2 & 1 \\ 0 & 1 & -1 \end{bmatrix}, \\
B_e &= \begin{bmatrix} \frac{1}{C_e} & 0 & -\frac{1}{C_e} \end{bmatrix}^\top.
\end{aligned}$$

The solution to (B.1) under a constant current I is

$$V_e(t) = e^{A_e t} V_e(0) + \int_0^t e^{A_e (t-\tau)} d\tau \cdot B_e I. \tag{B.2}$$

The eigenvalues of Ω_e are $0, -1, -3$, respectively. By the Cayley–Hamilton theorem, it follows that

$$e^{A_e t} = \left[\Psi^{-1}\psi(\mu_e, t)\right] \otimes \Omega_e, \tag{B.3}$$

where

$$\Psi = \begin{bmatrix} 1 & 0 & 0 \\ 1 & -1 & 1 \\ 1 & -3 & 9 \end{bmatrix},$$
$$\psi(\mu_e, t) = \begin{bmatrix} 1 & e^{-\mu_e t} & e^{-3\mu_e t} \end{bmatrix}^\top.$$

Based on (B.3), we can derive that

$$V_e(t) = \left[\Psi^{-1}\psi(\mu_e, t)\right] \otimes \Omega_e \cdot V_e(0) + \left[\Psi^{-1}\left(\bar{\psi}(\mu_e, t) - \bar{\psi}(\mu_e, 0)\right)\right] \otimes \Omega_e \cdot B_e I, \tag{B.4}$$

where

$$\bar{\psi}(\mu_e, t) = \begin{bmatrix} t & -\frac{e^{-\mu_e t}}{\mu_e} & -\frac{e^{-3\mu_e t}}{3\mu_e} \end{bmatrix}^\top.$$

With (B.4), one can extract $V_{e,1}$ and $V_{e,3}$ from V_e.

References

[1] Gregory L Plett. *Battery Management Systems, Volume I: Battery Modeling*. Artech House, 2015.

[2] Nalin A Chaturvedi, Reinhardt Klein, Jake Christensen, Jasim Ahmed, and Aleksandar Kojic. Algorithms for advanced battery-management systems. *IEEE Control Systems Magazine*, 30 (3):49–68, 2010.

[3] Yebin Wang, Huazhen Fang, Lei Zhou, and Toshihiro Wada. Revisiting the state-of-charge estimation for lithium-ion batteries: A methodical investigation of the extended Kalman filter approach. *IEEE Control Systems Magazine*, 37(4):73–96, 2017.

[4] Languang Lu, Xuebing Han, Jianqiu Li, Jianfeng Hua, and Minggao Ouyang. A review on the key issues for lithium-ion battery management in electric vehicles. *Journal of Power Sources*, 226:272–288, 2013.

[5] Yujie Wang, Jiaqiang Tian, Zhendong Sun, Li Wang, Ruilong Xu, Mince Li, and Zonghai Chen. A comprehensive review of battery modeling and state estimation approaches for advanced battery management systems. *Renewable and Sustainable Energy Reviews*, 131: 110015, 2020.

[6] C. D. Rahn and C.-Y. Wang. *Battery Systems Engineering*. Wiley, 2013.

[7] Huazhen Fang, Yebin Wang, Zafer Sahinoglu, Toshihiro Wada, and Satoshi Hara. State of charge estimation for lithium-ion batteries: An adaptive approach. *Control Engineering Practice*, 25:45 – 54, 2014.

[8] Venkatasailanathan Ramadesigan, Paul W. C. Northrop, Sumitava De, Shriram Santhanagopalan, Richard D. Braatz, and Venkat R. Subramanian. Modeling and simulation of

lithium-ion batteries from a systems engineering perspective. *Journal of The Electrochemical Society*, 159(3):R31–R45, 2012.

[9] Marc Doyle, Thomas F. Fuller, and John Newman. Modeling of galvanostatic charge and discharge of the lithium/polymer/insertion cell. *Journal of The Electrochemical Society*, 140 (6):1526–1533, 1993.

[10] Gang Ning and Branko N. Popov. Cycle life modeling of lithium-ion batteries. *Journal of The Electrochemical Society*, 151(10):A1584, 2004.

[11] M. Guo, G. Sikha, and R. White. Single-particle model for a lithium-ion cell: Thermal behavior. *Journal of The Electrochemical Society*, 158(2):A122, 2011.

[12] Tanvir R. Tanim, Christopher D. Rahn, and Chao-Yang Wang. State of charge estimation of a lithium ion cell based on a temperature dependent and electrolyte enhanced single particle model. *Energy*, 80:731–739, 2015. ISSN 0360-5442.

[13] Saeed K. Rahimian, Sean Rayman, and Ralph E. White. Extension of physics-based single particle model for higher charge–discharge rates. *Journal of Power Sources*, 224:180–194, 2013. ISSN 0378-7753.

[14] Scott J. Moura, Federico B. Argomedo, Reinhardt Klein, Anahita Mirtabatabaei, and Miroslav Krstic. Battery state estimation for a single particle model with electrolyte dynamics. *IEEE Transactions on Control Systems Technology*, 25(2):453–468, 2017.

[15] X. Han, M. Ouyang, L. Lu, and J. Li. Simplification of physics-based electrochemical model for lithium ion battery on electric vehicle. part I: Diffusion simplification and single particle model. *Journal of Power Sources*, 278:802–813, 2015. ISSN 0378-7753.

[16] Scott G. Marquis, Valentin Sulzer, Robert Timms, Colin P. Please, and S. Jon Chapman. An asymptotic derivation of a single particle model with electrolyte. *Journal of The Electrochemical Society*, 166(15):A3693, 2019.

[17] Jie Li, Nima Lotfi, Robert G. Landers, and Jonghyun Park. A single particle model for lithium-ion batteries with electrolyte and stress-enhanced diffusion physics. *Journal of The Electrochemical Society*, 164(4):A874–A883, 2017.

[18] Jie Li, K. Adewuyi, Nima Lotfi, Robert G. Landers, and Jonghyun Park. A single particle model with chemical/mechanical degradation physics for lithium ion battery state of health (SOH) estimation. *Applied Energy*, 212:1178–1190, 2018.

[19] Krishnakumar Gopalakrishnan and Gregory J. Offer. A composite single particle lithium-ion battery model through system identification. *IEEE Transactions on Control Systems Technology*, 30(1):1–13, 2022.

[20] Giacomo Saccani, Gabriele Ciaramella, and Davide M. Raimondo. A computationally efficient implementation of a battery pack electrochemical model using waveform relaxation. *Journal of Energy Storage*, 46:103758, 2022.

[21] Alexander Farmann and Dirk Uwe Sauer. Comparative study of reduced order equivalent circuit models for on-board state-of-available-power prediction of lithium-ion batteries in electric vehicles. *Applied Energy*, 225:1102–1122, 2018.

[22] H. He, R. Xiong, and J. Fan. Evaluation of lithium-ion battery equivalent circuit models for state of charge estimation by an experimental approach. *Energies*, 4:582–598, 2011.

[23] Sayed Mohammad Mousavi G. and M. Nikdel. Various battery models for various simulation studies and applications. *Renewable and Sustainable Energy Reviews*, 32:477–485, 2014.

[24] Ning Tian, Yebin Wang, Jian Chen, and Huazhen Fang. One-shot parameter identification of the thevenin's model for batteries: Methods and validation. *Journal of Energy Storage*, 29: 101282, 2020.

[25] Gregory L. Plett. Extended Kalman filtering for battery management systems of LiPB-based

HEV battery packs: Part 2. modeling and identification. *Journal of Power Sources*, 134(2): 262–276, 2004.

[26] Kuan-Ting Lee, Min-Jhen Dai, and Chiung-Cheng Chuang. Temperature-compensated model for lithium-ion polymer batteries with extended Kalman filter state-of-charge estimation for an implantable charger. *IEEE Transactions on Industrial Electronics*, 65(1):589–596, 2018.

[27] Min Chen and G.A. Rincon-Mora. Accurate electrical battery model capable of predicting runtime and I-V performance. *IEEE Transactions on Energy Conversion*, 21(2):504–511, 2006.

[28] Xiaosong Hu, Shengbo Li, and Huei Peng. A comparative study of equivalent circuit models for Li-ion batteries. *Journal of Power Sources*, 198:359–367, 2012.

[29] Caihao Weng, Jing Sun, and Huei Peng. A unified open-circuit-voltage model of lithium-ion batteries for state-of-charge estimation and state-of-health monitoring. *Journal of Power Sources*, 258:228–237, 2014.

[30] Ning Tian, Huazhen Fang, Jian Chen, and Yebin Wang. Nonlinear double-capacitor model for rechargeable batteries: Modeling, identification, and validation. *IEEE Transactions on Control Systems Technology*, 29(1):370–384, 2020.

[31] Ning Tian, Huazhen Fang, and Jian Chen. A new nonlinear double-capacitor model for rechargeable batteries. In *Proceedings of the 44th Annual Conference of the IEEE Industrial Electronics Society*, pages 1613–1618, 2018.

[32] Hamidreza Movahedi, Ning Tian, Huazhen Fang, and Rajesh Rajamani. Hysteresis compensation and nonlinear observer design for state-of-charge estimation using a nonlinear double-capacitor li-ion battery model. *IEEE/ASME Transactions on Mechatronics*, 27(1):594–604, 2022.

[33] Alan G. Li, Karthik Mayilvahanan, Alan C. West, and Matthias Preindl. Discrete-time modeling of li-ion batteries with electrochemical overpotentials including diffusion. *Journal of Power Sources*, 500:229991, 2021.

[34] Chuanxin Fan, Kieran O'Regan, Liuying Li, Matthew D. Higgins, Emma Kendrick, and Widanalage D. Widanage. Data-driven identification of lithium-ion batteries: A nonlinear equivalent circuit model with diffusion dynamics. *Applied Energy*, 321:119336, 2022.

[35] Zhimin Xi, Modjtaba Dahmardeh, Bing Xia, Yuhong Fu, and Chris Mi. Learning of battery model bias for effective state of charge estimation of lithium-ion batteries. *IEEE Transactions on Vehicular Technology*, 68(9):8613–8628, 2019.

[36] Hao Tu, Scott Moura, Yebin Wang, and Huazhen Fang. Integrating physics-based modeling with machine learning for lithium-ion batteries. *Applied Energy*, 329:120289, 2023.

[37] Yangsheng Hu, Raymond A. de Callafon, Ning Tian, and Huazhen Fang. Tensor network-based mimo volterra model for lithium-ion batteries. *IEEE Transactions on Control Systems Technology*, 2023. in press.

[38] Alexander Bills, Shashank Sripad, William L Fredericks, Matthew Guttenberg, Devin Charles, Evan Frank, and Venkatasubramanian Viswanathan. Universal battery performance and degradation model for electric aircraft. *arXiv preprint arXiv:2008.01527*, 2020.

[39] Nikhil Biju and Huazhen Fang. Battx: An equivalent circuit model for lithium-ion batteries over broad current ranges. *Applied Energy*, 339:120905, 2023.

[40] Nikhil Biju and Huazhen Fang. On the design of an equivalent circuit model for lithium-ion batteries operating across broad current ranges. In *Proceedings of the 22nd IFAC World Congress*, 2023.

[41] Xinfan Lin, Hector Perez, Shankar Mohan, Jason Siegel, Anna Stefanopoulou, Yi Ding,

and Matthew Castanier. A lumped-parameter electro-thermal model for cylindrical batteries. *Journal of Power Sources*, 257:1–11, 07 2014.

[42] Rohit Mehta and Amit Gupta. An improved single-particle model with electrolyte dynamics for high current applications of lithium-ion cells. *Electrochimica Acta*, 389:138623, 2021.

[43] Huazhen Fang, Yebin Wang, and Jian Chen. Health-aware and user-involved battery charging management for electric vehicles: Linear quadratic strategies. *IEEE Transactions on Control Systems Technology*, 25(3):911–923, 2017.

[44] Xing Xu, Wei Wang, and Long Chen. Order reduction of lithium-ion battery model based on solid state diffusion dynamics via large scale systems theory. *Journal of The Electrochemical Society*, 163(7):A1429–A1441, 2016.

[45] Gamma Technologies, LLC. *GT-SUITE User Manual*. Gamma Technologies, Westmont,IL,USA,2022, 2022.

[46] Karen E Thomas and John Newman. Thermal modeling of porous insertion electrodes. *Journal of the Electrochemical Society*, 150(2):A176, 2003.

[47] Christophe Forgez, Dinh Vinh Do, Guy Friedrich, Mathieu Morcrette, and Charles Delacourt. Thermal modeling of a cylindrical lifepo4/graphite lithium-ion battery. *Journal of Power Sources*, 195(9):2961–2968, 2010.